# DEVELOPMENT OF A FREE-VORTEX WAKE MODEL IN STATE-SPACE FORM

Patrick Betoney*, Roberto Celi†, and J. Gordon Leishman‡
Department of Aerospace Engineering
University of Maryland, College Park, MD 20742, USA

**Abstract**

The paper describes the initial development of a free-vortex rotor wake model in state-space form, which is based on the principles of vorticity transport. The governing wake equations are formulated as partial differential equations and are converted into a system of ordinary differential equations by the method of lines. The states of the model are the time varying positions in space of collocation points on the wake filaments. Linearized models are extracted numerically using finite-difference approximations. The resulting state-space models are large and order reduction is important. Three techniques are described where the state vector is approximated by a series of shape functions. The new state-space wake is validated in five different flight conditions by comparison with an existing finite-difference wake that implements the same fluid dynamics model. Results are also presented for a coupled model including the free-vortex wake, unsteady airfoil aerodynamics, and rotor blade flapping. Open loop poles of the coupled linearized system are also shown. The agreement with the finite-difference wake geometries is uniformly excellent within about half a rotor radius but deteriorates slightly further downstream in some flight conditions, although blade inflow and lift are not affected. Substantial reductions in the number of states are shown to be possible without significant degradation of accuracy.

**List of Symbols**

| | |
|---|---|
| $A$ | State matrix |
| $A_1, A_2, b_1, b_2$ | Coefficients of unsteady airfoil model |
| $B$ | Control matrix |
| $c$ | Blade chord |
| $C_l$ | Airfoil lift coefficient |
| $C_l^{nc}, C_l^c$ | Noncirculatory and circulatory portions of the airfoil lift coefficient |
| $C_{l_\alpha}$ | Airfoil lift curve slope |
| $\dot{h}$ | Airfoil plunge velocity |
| $L(y)$ | Blade lift per unit span |
| $M_\beta$ | Aerodynamic flapping moment |
| $\mathbf{r}$ | Position vector of point on vortex filament |
| $r_x, r_y, r_z$ | Components of $\mathbf{r}$ in rotor coordinate system |
| $r_v$ | Spanwise position of vortex release point |
| $R$ | Rotor radius |
| $\mathbf{u}$ | Vector of controls |
| $V$ | Cross-sectional free-stream velocity |
| $\mathbf{V}$ | Local convection velocity of the vortex |
| $\Delta w_g$ | Vertical velocity perturbation in airfoil unsteady aerodynamic model |
| $\mathbf{x}$ | Vector of states |
| $x_1, x_2$ | States of airfoil unsteady aerodynamic model |
| $\mathbf{x}_{AC}, \mathbf{x}_{FW}$ | Partitions of $\mathbf{x}$ containing aircraft and free wake states |
| $z_1, z_2$ | States of airfoil unsteady aerodynamic model |
| $\alpha$ | Instantaneous airfoil angle of attack |
| $\alpha_s, \beta_0$ | Rotor shaft angle and flapping angle |
| $\beta, \beta_i$ | Flapping angle of generic blade and of $i$-th blade |
| $\Gamma_b$ | Bound circulation |
| $\Gamma_v$ | Circulation strength of the tip vortex |
| $\Delta(\ldots)$ | Small increment for finite-difference calculations |
| $\zeta$ | Angular distance of a vortex point from the blade (wake age) |
| $\lambda_i$ | Inflow velocity along $\mathbf{k}$, nondimensional |
| $\mu$ | Advance ratio |
| $\psi$ | Blade azimuth angle |
| $\Omega$ | Rotor speed |
| $(\overset{*}{\ldots})$ | Derivative with respect to $\psi, \partial(\ldots)/\partial\psi$ |

**Abbreviations**

| | |
|---|---|
| CFD | Computational Fluid Dynamics |
| CSD | Computational Structural Dynamics |
| DAE | Differential-Algebraic Equation |
| MOL | Method of Lines |
| ODE | Ordinary Differential Equation |
| PC2B | Predictor-Corrector 2nd-Order Backward Difference scheme |
| PDE | Partial Differential Equation |

## 1. Introduction

Advanced rotor control technologies have been proposed to improve the performance, aeromechanical stability, loads and vibrations, and handling qualities of rotorcraft. These devices include individual blade control, trailing edge flaps, elevons, and morphing airfoils, and generate localized, but very powerful, aerodynamic effects that significantly affect all aspects of rotorcraft dynamics. Because the effects are localized, they cannot be rigorously modeled with momentum-like theories that consider the rotor as an actuator disk, and vortex wake type methods need to be used. From the point of view of the control designer, a technical barrier is that existing vortex wake models are not formulated in state-space

*Graduate Research Assistant, pbetoney@umd.edu.
†Professor, celi@umd.edu.
‡Minta Martin Professor, leishman@umd.edu.
Paper presented at the 35th European Rotorcraft Forum, Hamburg, Germany, September 22-26, 2009; 

form, therefore they cannot be used when a linearized, i.e., $(A, B, C, D)$ model is required. In fact, the most powerful control analysis and synthesis methodologies currently being used require that the model of the plant (i.e, of the system to be controlled) be in the form of systems of ordinary differential equations. Finite difference-based wake solution methodologies are very cumbersome if not outright impossible to use.

Furthermore, without a wake state-space model it is not possible to formulate a linearized state-space model of the complete rotorcraft, and so it is not possible to directly assess open- and closed-loop aeroelastic and flight dynamic stability from the eigenvalues of the linearized system (or from its characteristic exponents if the system has periodic coefficients and Floquet theory is used). In this case, stability can only be assessed indirectly from an examination of time histories.

It is also not possible to directly extract Bode plots to describe, for example, the frequency response of the rotor to active control inputs, or the rigid body response to pilot inputs, which are important for handling qualities analyses and specification compliance. Currently, the only way to reconstruct some of this information is through system identification techniques applied to experimental (e.g., [1]) or simulated (e.g., [2, 3]) time histories.

Another solution is to rely on simplified, linearized wake models that can be cast in state-space form. These models are based on the solution of the fluid dynamics equations over global domains. These are small-disturbance, momentum theory based solutions, which represent in a gross way the effects of certain rotor parameters on the rotor inflow. Such models include all classes of the actuator disk theories.

Because of the underlying physics, these widely used theories have significant limitations. For example, two of the most popular models, the "dynamic inflow" model [4] and the "finite state wake" [5], and their numerous subsequent developments, trace their origins directly to the small disturbance, acceleration potential solution over a disk by Joglekar and Loewy [6]. As solutions over a disk, they intrinsically lack the resolution required to model local details of the flow field. Their extension to maneuvers requires *ad hoc* assumptions about how the wake geometries change. They also assume that the perturbations at the rotor disk are small compared with the relative free-stream velocity, which implies that the rotor is lightly loaded. For the same reason, such theories cannot rigorously model large amplitude maneuvers, especially when the wake vortices tend to merge or bundle. As actuator disk theories, they implicitly require the presence of a fully developed slipstream that can be assumed to encompass the limits of the physical rotor disk. For this reason, and because they are small perturbation theories, they cannot rigorously model steep descents and the vortex ring state. Finally, because they are fundamentally solutions for a single rotor, they cannot model the complex interactions associated with multi-rotor configurations, and do not contain the physics of the wake distortions from rotor-fuselage or rotor-empennage interactions.

These theories are very popular both for their computational efficiency, and because they often can produce good results for many conditions of practical interest. However, it is clear that the current inability to write a complete rotorcraft mathematical model in the form of a system of ODEs with a free-vortex wake, is a significant gap in the state-of-the-art in several areas of helicopter analysis. Therefore, the main objective of the present research is to help close this gap by deriving a first principles-based mathematical model of free-vortex wakes in the form of a set of ODEs.

Current state-of-the-art free-vortex wake models, which include those by Brown [7], Johnson [8], Leishman [9], and their coworkers, are capable of accurately modeling complex, multi-rotor interactions under any flight condition, including the vortex ring state and in ground effect. The state-space wake model described in the present paper is based on that of Ref. [9].

The only previous state-space free-vortex wake model available in the literature is that by Johnson, Refs. [10, 11]. In this model, the states are generalized coordinates describing the inflow, and the inputs are generalized coordinates describing the circulation. It requires the calculation of an impulse response of the wake-induced downwash $\lambda$ to the rate of change of circulation with time for the shed wake, and of an impulse response of $\lambda$ to circulation for the trailed wake. In hover, this is done using frequency domain system identification techniques. Ref. [11] is limited to the case of hover, Ref. [10] also briefly covers forward flight. For the hover case, results for both an undistorted helical wake geometry and a distorted, prescribed geometry are presented [10, 11]. In forward flight, because the wake geometry is time-varying, so are the impulse responses of $\lambda$. Then, it is suggested to use a procedure based on Ref. [12], where through some simplifying assumptions it is possible to obtain analytical solutions for the induced velocities from the wake, and therefore reconstruct the required time-varying impulse responses. The study was described as a "feasibility investigation," and no further material was published.

In Ref. [13], the same governing free-vortex equations of Ref. [9] were converted to a system of ODEs using the Method of Lines (MOL). The states were the time-varying spatial positions of collocation points on the wake vortices. The objective of the paper was to study some basic features of the MOL methodology, and so only the very simple rigid wake case was considered; the true vortex dynamics and the mutual interactions between blade and wake vortices were not modeled in this case.

The MOL, as used in Ref. [13], is a numerical technique for the solution of PDEs in which all but one dimension is discretized, usually the time-dimension, resulting in a system of ODEs in this dimension. The method has been applied to the Navier–Stokes equations [14, 15, 16], and, in particular, to the vorticity transport equations by Tokunaga *et al.* [17, 18].

Representations of vortices in state-space form have been implemented in other areas, such as the modeling of leading edge vortices in delta wings at high angle-of-attack [19, 20, 21], as they are very important for accurate prediction of lift and rolling moments, and for the design of feedback flow control. These models are simplified, low-order representations of trailed vortices that are depicted as straight-line segments starting from some initial point near the nose to the vortex breakdown location. The overall system is nonlinear, and the states of the model are the breakdown position along each axis and vortex strength of both

the left and right vortices.

Vortex lattice methods have been used to develop two-dimensional [22, 23] and three-dimensional [24] unsteady aerodynamic models in state-space form. The states in this case are the circulation strengths of each vortex segment, but the lattice (or wake) is fixed and is not allowed to convect under its own induced velocities. Reduced-order models are also considered by transforming the model into balanced coordinates and truncating states which are less significant. Other representations of vortices as a set of ODEs include the point-vortex models [25, 26]. As the name implies, these models represent the vorticity being shed from sharp edges as discrete points in a 2D flow. They are capable of modeling complex fluid-solid interactions that allow accurate simulation and control of both the body and its surrounding flow. However, their extension to 3D is either not possible or has not been realized.

In light of the preceding discussion, the objectives of the present paper are:

1. To present the initial results of the development of the state-space version of a time-accurate, first principles-based, free-vortex rotor wake model, using the Method-of-Lines.
2. To discuss the extraction of a linearized model of the free-vortex wake in the mathematical form:

   $$\dot{\mathbf{x}} = A\mathbf{x} + B\mathbf{u}$$

   where $\mathbf{x}$ and $\mathbf{u}$ are, respectively, vectors of states and controls.
3. To present comparisons between the new state-space free-vortex wake and an existing finite-difference version, based on the same governing equations, for the calculation of converged wake geometries and of wake transients, and for models that also include airfoil unsteady aerodynamics, and rotor blade flapping.
4. To present techniques to reduce the size of the state-space free-vortex wake model through series of approximate shape functions, and to compare full- and reduced-order results.

## 2. Mathematical model

The State-Space Free vortex Wake (SSFW) model described in the present paper is based on recasting into state-space form the Maryland Free Wake (MFW) model. The MFW has been extensively described in the literature [9, 27]. Therefore, only the MFW features relevant to the development of the SSFW will be presented here.

### 2.1. Vortex model

The MFW is based on a vortex discretization, in which the geometry of the vortex filaments is governed by the principles of vorticity transport and is described by the following PDEs [28]

$$\frac{\partial \mathbf{r}(\psi,\zeta)}{\partial \psi} + \frac{\partial \mathbf{r}(\psi,\zeta)}{\partial \zeta} = \frac{1}{\Omega}\mathbf{V}[\mathbf{r}(\psi,\zeta)] \tag{1}$$

where $\mathbf{r}$ is a position vector describing the geometry of each of the vortices comprising the wake (trailed or shed), $\psi$ is the blade azimuth, $\zeta$ is the wake age, i.e., the time elapsed since the release of the vortex element into the flow field (expressed as an angular distance from the blade release point), $\Omega$ is the rotor speed, and $\mathbf{V}$ is the local convection velocity of the vortex filament. The velocity term on the right-hand-side is given by [29]:

$$\mathbf{V}[\mathbf{r}(\psi,\zeta)] = \mathbf{V}_\infty + \mathbf{V}_{\mathrm{ind}}[\mathbf{r}(\psi,\zeta)] + \mathbf{V}_{\mathrm{man}}[\mathbf{r}(\psi,\zeta)] \tag{2}$$

where $\mathbf{V}_\infty$ is the free-stream velocity resulting from the linear motion of the helicopter, $\mathbf{V}_{\mathrm{ind}}$ is the inflow velocity from the self- and mutually-induced velocities of the trailed vortices and the blade bound circulation and $\mathbf{V}_{\mathrm{man}}$ is the portion of the free-stream velocity associated with the rotational motion of the helicopter. In the present study, only the first two terms are considered, but the methodology is set up to rigorously handle any type of maneuver.

The induced velocity term in Eq. (2) is calculated by straight-line vortex segmentation with a finite core size $r_c$ to remove the singularity at the vortex axis. This is equivalent to calculating the induced velocites using the Biot–Savart law with a trapezoidal numerical quadrature. The induced velocity at a generic point is represented by the following summation:

$$\begin{aligned}\mathbf{V}_{\mathrm{ind}} = &\sum_{j=1}^{N_{vf}}\sum_{k=1}^{k_{max}}\left[\frac{\Gamma_v}{4\pi}\frac{h(\cos\theta_1-\cos\theta_2)}{\left(r_c^4+h^4\right)^{1/2}}\right]_{j,k}\mathbf{e}_{j,k}\\ &+\sum_{j=1}^{N_b}\sum_{i=1}^{i_{max}}\left[\frac{\Gamma_b}{4\pi}\frac{h(\cos\theta_1-\cos\theta_2)}{\left(r_c^4+h^4\right)^{1/2}}\right]_{j,i}\mathbf{e}_{j,i}\end{aligned} \tag{3}$$

where $N_{vf}$ is the number of vortex filaments, $N_b$ is the number of blades, and $k_{max}$ and $i_{max}$ are the number of segments along each vortex and blade, respectively. The trailed and blade bound circulations are $\Gamma_v$ and $\Gamma_b$, respectively. The perpendicular separation distance between the vortex filament and a generic point is $h$; the included angles are $\theta_1$ and $\theta_2$, and the unit vector $\mathbf{e}$ gives the direction of the velocity vector at the point (see Ref. [30], Ch. 10, for a more detailed discussion). The first term on the right-hand-side of Eq. (3) represents the contribution to the induced velocity from the trailed vortices, while the second term represents the contribution from the blade bound circulation.

In the MFW, the governing equations, Eq. (1), are discretized using finite-difference approximations in blade azimuth $\psi$ and wake age $\zeta$. The $\psi$-derivative is based on a second-order, predictor-corrector, backward difference scheme (denoted as PC2B). Its approximation uses three previous azimuth steps and is given by [27]:

$$\begin{aligned}\frac{\partial \mathbf{r}}{\partial \psi} \approx \left.\frac{d\mathbf{r}}{d\psi}\right|_{\psi+\Delta\psi/2,\zeta}&\\ =\frac{1}{4\Delta\psi}\big(&3\mathbf{r}(\psi+\Delta\psi,\zeta)-\mathbf{r}(\psi,\zeta)\\ &-3\mathbf{r}(\psi-\Delta\psi,\zeta)+\mathbf{r}(\psi-2\Delta\psi,\zeta)\big)\end{aligned} \tag{4}$$

The approximation of the $\zeta$-derivative uses a five-point central difference and is given by:

$$\begin{aligned}\frac{\partial \mathbf{r}}{\partial \zeta} \approx \left.\frac{d\mathbf{r}}{d\psi}\right|_{\psi+\Delta\psi/2,\zeta+\Delta\zeta/2}&\\ =\frac{1}{2\Delta\psi}\big(&\mathbf{r}(\psi+\Delta\psi,\zeta+\Delta\zeta)-\mathbf{r}(\psi+\Delta\psi,\zeta)\\ &+\mathbf{r}(\psi,\zeta+\Delta\zeta)-\mathbf{r}(\psi,\zeta)\big)\end{aligned} \tag{5}$$

The derivatives in Eqs. (4) and (5) are computed at the midpoint of the $\psi-\zeta$ square grid. Therefore, the $\psi$-derivative at the cell center is based on the values at both $\zeta$ and $\zeta+\Delta\zeta$.

The MFW is capable of modeling both the shed and the trailed portions of the wake, and there is no limitation on the number of vortices used to discretize either portion. However, in the present study, only a trailed wake modeled by a single tip vortex per blade will be included, for both the MFW and the SSFW. The shed wake effects will be modeled through an unsteady airfoil aerodynamic model.

## 2.2. State-Space Free-Vortex Wake Model

The SSFW is obtained by discretizing the governing equations with respect to wake age $\zeta$ only, which results in a system of ODEs in blade azimuth $\psi$. The specific form of this system depends on the finite-difference discretization chosen. In the present study, a fourth-order five-point biased upwind approximation (5PBU4) [31] is used. With this scheme, Eq. (1) becomes:

$$\begin{aligned}\frac{\partial r_k(\psi,\zeta_i)}{\partial\psi} = -\frac{1}{12\Delta\zeta}\Big[ &- r_k(\psi,\zeta_i-3\Delta\zeta)\\ &+ 6r_k(\psi,\zeta_i-2\Delta\zeta) - 18r_k(\psi,\zeta_i-\Delta\zeta)\\ &+ 10r_k(\psi,\zeta_i) + 3r_k(\psi,\zeta_i+\Delta\zeta)\Big]\\ &+ \frac{1}{\Omega}V_k(\psi,\zeta_i)\end{aligned} \tag{6}$$

which is an ODE in $r_k(\psi,\zeta_i)$. The subscript $k$ denotes any of the three coordinate directions, e.g., $(1,2,3)=(x,y,z)$. At the two ends of the $\zeta$-domain, slightly different discretizations are needed. These are [31]

$$\begin{aligned}\frac{\partial r_k(\psi,\zeta_1)}{\partial\zeta} \approx \frac{1}{12\Delta\zeta}\Big[ &- 25r_k(\psi,\zeta_1) + 48r_k(\psi,\zeta_2)\\ &- 36r_k(\psi,\zeta_3) + 16r_k(\psi,\zeta_4) + 3r_k(\psi,\zeta_5)\Big]\end{aligned} \tag{7}$$

$$\begin{aligned}\frac{\partial r_k(\psi,\zeta_2)}{\partial\zeta} \approx \frac{1}{12\Delta\zeta}\Big[ &- 3r_k(\psi,\zeta_1) + 10r_k(\psi,\zeta_2)\\ &+ 18r_k(\psi,\zeta_3) - 6r_k(\psi,\zeta_4) + r_k(\psi,\zeta_5)\Big]\end{aligned} \tag{8}$$

$$\begin{aligned}\frac{\partial r_k(\psi,\zeta_3)}{\partial\zeta} \approx \frac{1}{12\Delta\zeta}\Big[ &r_k(\psi,\zeta_1) - 8r_k(\psi,\zeta_2)\\ &+ 8r_k(\psi,\zeta_4) - r_k(\psi,\zeta_5)\Big]\end{aligned} \tag{9}$$

and

$$\begin{aligned}\frac{\partial r_k(\psi,\zeta_{N_\zeta})}{\partial\zeta} \approx \frac{1}{12\Delta\zeta}[ &3r_k(\psi,\zeta_{N_\zeta-3})\\ &- 16r_k(\psi,\zeta_{N_\zeta-2}) + 36r_k(\psi,\zeta_{N_\zeta-1})\\ &- 48r_k(\psi,\zeta_{N_\zeta}) + 25r_k(\psi,\zeta_{N_\zeta+1})],\end{aligned} \tag{10}$$

where $N_\zeta$ is the number of collocation points if the domain is split into $N_\zeta-1$ intervals. Combining Eqs. (6) for all interior collocation points and Eqs. (7) through (10) at the ends of the domain results in a system of $N_\zeta$ ODEs describing the wake geometry along any spatial axis $k$:

$$\dot{\mathbf{r}}_k(\psi,\boldsymbol{\zeta}) = -[A_\zeta]\mathbf{r}_k(\psi,\boldsymbol{\zeta}) + \frac{1}{\Omega}\mathbf{V}_k[\mathbf{r}(\psi)] \tag{11}$$

This semi-discretization is generally known as the method of lines. In Eq. (11), $\dot{(\,)}=\partial/\partial\psi$, $\boldsymbol{\zeta}=[\ \zeta_1\quad\zeta_2\quad\dots\quad\zeta_{N_\zeta}\ ]^T$ is the vector containing the wake age values of the $N_\zeta$ collocation points that describe the geometry of the vortex, and $[A_\zeta]$ is a finite-difference matrix, the specific form of which depends on the $\zeta$-discretization scheme used. In this case, the finite-difference matrix takes the values of the leading coefficients of the 5PBU4 scheme (see Refs. [13, 31] for a more detailed description of the differencing schemes), i.e.,

$$[A_\zeta] = \frac{1}{12\Delta\zeta}\begin{bmatrix} -25 & 48 & -36 & 16 & 3 & & \\ -3 & 10 & 18 & -6 & 1 & & \\ 1 & -8 & 0 & 8 & -1 & & \\ -1 & 6 & -18 & 10 & 3 & & \\ & \dots & \dots & \dots & \dots & \dots & \\ & & -1 & 6 & -18 & 10 & 3\\ & & 3 & -16 & 36 & -48 & 25 \end{bmatrix} \tag{12}$$

where all the terms outside the diagonal band are equal to zero. Regardless of the specific $\zeta$-discretization used, the resulting system of ODEs has the same general form as Eq. (11). Only the values of the constant coefficient matrix $[A_\zeta]$ change with different discretization schemes.

The complete state-space model couples the system of ODEs in Eq. (11) for all three spatial components, and thus, the governing wake equations for each vortex (trailed or shed) are

$$\begin{Bmatrix} \dot{\mathbf{r}}_x(\psi,\boldsymbol{\zeta}) \\ \dot{\mathbf{r}}_y(\psi,\boldsymbol{\zeta}) \\ \dot{\mathbf{r}}_z(\psi,\boldsymbol{\zeta}) \end{Bmatrix} = \begin{bmatrix} [A_\zeta] & 0 & 0 \\ 0 & [A_\zeta] & 0 \\ 0 & 0 & [A_\zeta] \end{bmatrix} \times \begin{Bmatrix} \mathbf{r}_x(\psi,\boldsymbol{\zeta}) \\ \mathbf{r}_y(\psi,\boldsymbol{\zeta}) \\ \mathbf{r}_z(\psi,\boldsymbol{\zeta}) \end{Bmatrix} + \begin{Bmatrix} \mathbf{V}_x[\mathbf{r}(\psi)] \\ \mathbf{V}_y[\mathbf{r}(\psi)] \\ \mathbf{V}_z[\mathbf{r}(\psi)] \end{Bmatrix} \tag{13}$$

Equation (13) needs to be written as many times as there are wake vortices. The coupling among the vortices is then introduced by the velocity terms $\mathbf{V}_k[\mathbf{r}(\psi)]$. The solution of the system of ODEs yields the solution of the original PDEs. The quantities $r_k(\psi,\zeta_i), i=1,2,\dots,N_\zeta$ become the states of the model. Each $r_k(\psi,\zeta_i)$ represents the position of a collocation point on a vortex filament along the $x$-, $y$- or $z$-axis.

It should be noted that, because the velocity vectors $\mathbf{V}_k$ on the right-hand-side of the governing equations are not affected by the finite-difference discretization, they are treated identically in the SSFW and the MFW. This simplifies considerably the computer implementation of the wake model because much of the computational and implementation effort lies in the proper handling of those vectors, which can be shared between the two wake formulations.

The equation of vorticity transport, Eq. (1), is first-order in $\psi$ and $\zeta$. Therefore, it requires an initial condition and a boundary condition. In Ref. [13], the initial and boundary conditions were taken from the exact solution to the rigid wake problem. The same approach is taken here for the initial conditions, with the only exception that the dependency on the shaft angle is removed (because of a rotation of the coordinate system by the shaft angle). The boundary conditions are based on the instantaneous tip position of each blade. The initial conditions for all three spatial components

are thus:

$$r_x(0,\zeta) = R\mu\zeta + r_v \cos\beta_0 \cos\zeta \tag{14}$$

$$r_y(0,\zeta) = -r_v \cos\beta_0 \sin\zeta \tag{15}$$

$$r_z(0,\zeta) = R\lambda_i\zeta + r_v \sin\beta_0 \tag{16}$$

The boundary conditions for all three components are:

$$r_x(\psi,0) = r_v \cos\beta\cos\psi \tag{17}$$

$$r_y(\psi,0) = r_v \cos\beta\sin\psi \tag{18}$$

$$r_z(\psi,0) = r_v \sin\beta \tag{19}$$

where $\beta = \beta(\psi)$.

### 2.3. Shed Wake Aerodynamics

For computational efficiency, the effects of the shed wake were captured in the present study by using an unsteady airfoil model. This model, which is valid for incompressible, attached flow, is described in detail in Ref. [30], therefore only the key features are summarized here. The model is used to calculate the aerodynamic coefficients at a given blade cross section, therefore, it must be repeated for a sufficient number of cross sections on each blade to obtain the spanwise airload distribution with the desired accuracy. The model is available in two equivalent mathematical forms, i.e., in state-space form and in finite-difference (recurrence) form. Either form can be used with both the MFW and the SSFW. However, for consistency, in the present paper the finite-difference form will be used with the MFW, and the state-space form with the SSFW.

#### 2.3.1. State-space Form

For arbitrary blade motion, the governing equations for the circulatory component $C_l^c$ of the lift at a blade cross section along the blade can be represented in state-space form as

$$\begin{Bmatrix} \dot{x}_1 \\ \dot{x}_2 \end{Bmatrix} = \begin{bmatrix} 0 & 1 \\ -b_1 b_2 \left(\frac{2V}{c}\right)^2 & (b_1+b_2)\left(\frac{2V}{c}\right) \end{bmatrix} \begin{Bmatrix} x_1 \\ x_2 \end{Bmatrix} + \begin{Bmatrix} 0 \\ 1 \end{Bmatrix} \alpha(t) \tag{20}$$

plus the output equation,

$$C_l^c(t) = \left[ b_1 b_2 \left(\frac{2V}{c}\right)^2 \quad (A_1 b_1 + A_2 b_2)\left(\frac{2V}{c}\right) \right] \begin{Bmatrix} x_1 \\ x_2 \end{Bmatrix} + C_{l_\alpha}(1 - A_1 - A_2)\alpha(t) \tag{21}$$

The coefficients $A_1, A_2, b_1$, and $b_2$ come from the R. T. Jones approximation to the Wagner function, where $A_1$ = 0.165, $A_2$ = 0.335, $b_1$ = 0.0455, and $b_2$ = 0.3, $V$ is the local flow velocity, $c$ is chord length, $\alpha$ is the instantaneous angle of attack, and $C_{l_\alpha}$ is the lift-curve-slope.

To represent the response to changes in the vertical gust velocity (which includes inflow perturbations), two additional aerodynamic states are needed at each blade station. The governing equations are similar to Eq. (20) except that the angle of attack is replaced by a perturbation in the vertical gust velocity $w_g$ over the local flow velocity $V$ (an approximate angle of attack). These equations represent the additional contributions to the circulatory component of the lift and are given in state-space form as

$$\begin{Bmatrix} \dot{z}_1 \\ \dot{z}_2 \end{Bmatrix} = \begin{bmatrix} 0 & 1 \\ -b_1 b_2 \left(\frac{2V}{c}\right)^2 & (b_1+b_2)\left(\frac{2V}{c}\right) \end{bmatrix} \times \begin{Bmatrix} z_1 \\ z_2 \end{Bmatrix} + \begin{Bmatrix} 0 \\ 1 \end{Bmatrix} \frac{\Delta w_g(t)}{V} \tag{22}$$

with the output equation

$$\Delta C_l^c(t) = \left[ b_1 b_2 \left(\frac{2V}{c}\right)^2 \quad (A_1 b_1 + A_2 b_2)\left(\frac{2V}{c}\right) \right] \times \begin{Bmatrix} x_1 \\ x_2 \end{Bmatrix} + C_{l_\alpha}(1 - A_1 - A_2)\frac{\Delta w_g(t)}{V} \tag{23}$$

The coefficients in this case are $A_1$ = 0.5, $A_2$ = 0.5, $b_1$ = 0.13, and $b_2$ = 1.0, which come from an approximation to the Küssner function.

#### 2.3.2. Finite Difference (Recursive) Form

In this formulation, the effects of the shed wake are represented by a change in the effective angle of attack, $\alpha_e$. Therefore, the circulatory component of the lift at each blade section can be represented simply as

$$[\Delta]\, C_l^c(s) = C_{l_\alpha}\alpha_e(s) \tag{24}$$

where the $\Delta$ is an optional symbol which represents the additional lift created by a gust perturbation $\Delta w_g$, and $s$ is the distance traveled by the airfoil in semichords, or

$$s = \frac{2Vt}{c} = \frac{2V}{c}\left(\frac{\psi}{\Omega}\right) \tag{25}$$

The effective angle of attack is given by the expression

$$\alpha_e(s) = \alpha(s) - X(s) - Y(s) \tag{26}$$

where $\alpha(s)$ is the instantaneous angle of attack on the blade element. The terms $X(s)$ and $Y(s)$ are one-step recursive formulas, which are based on the mid-point rule of integration, and contain all the time history information of the unsteady aerodynamics. They are given as

$$X(s) = X(s-\Delta s)e^{-b_1\Delta s} + A_1\Delta\alpha_s e^{-b_1\Delta s/2} \tag{27}$$

$$Y(s) = Y(s-\Delta s)e^{-b_2\Delta s} + A_2\Delta\alpha_s e^{-b_2\Delta s/2} \tag{28}$$

The coefficients $A_1, A_2, b_1$, and $b_2$, are the same as those used in the state-space formulation depending on whether we are dealing with arbitrary blade motion (Wagner's function) or vertical gust response (Küssner's function). Thus, the model consists of four recursive formulas at each blade station. The term $\Delta\alpha_s$ represents the change in angle of attack between successive steps, i.e.,

$$\Delta\alpha_s = \alpha(s) - \alpha(s-\Delta s) \tag{29}$$

### 2.3.3. Other Considerations

Along with the circulatory component of the lift, the non-circulatory part must also be considered. In coefficient form, this is expressed in Ref. [30] as

$$C_l^{nc} = \pi b \left( \frac{\dot{\alpha}}{V} + \frac{\ddot{h}}{V^2} - \frac{ba\ddot{\alpha}}{V^2} \right) \tag{30}$$

where $\ddot{h}$ is the plunging acceleration of the blade station, which is the result of flap motion, and $a$ is related to the position of the pitch axis (not the lift-curve-slope). The total lift coefficient is then the combination of the circulatory and non-circulatory components, or

$$C_l = C_l^c + \Delta C_l^c + C_l^{nc}. \tag{31}$$

From here, the lift per unit span at every blade station can be computed using the expression

$$L(y) = \frac{1}{2}\rho V^2(y) c C_l = \rho V(y) \Gamma_b(y) \tag{32}$$

which can also be formulated in terms of the blade bound circulation as shown. After rearranging, the bound circulation at every blade station becomes

$$\Gamma_b(y) = \frac{1}{2} V(y) c C_l = \frac{L(y)}{\rho V(y)} \tag{33}$$

where $\rho$ is the air density. Finally, the flapping moment acting on the blade is given by

$$M_\beta = \int_0^R L(y) y \, dy \tag{34}$$

and the circulation strength of the tip vortex is taken to be the maximum value of the bound circulation of the blade, i.e.,

$$\Gamma_v = \max \left[ \Gamma_b(y) \right] \tag{35}$$

## 2.4. Rotor Equations

The model used in the present study includes an elementary representation of rotor dynamics, in which the blades are assumed to be rigid, hinged at the axis of rotation, and possessing only the flap degree of freedom. The hub is assumed to be fixed, so that there is no dynamic coupling among the rotor blades. The governing equation for each blade is then simply

$$\overset{**}{\beta} + \beta = \frac{M_\beta}{I_\beta \Omega^2} \tag{36}$$

where $\overset{**}{(\,)} = \partial^2(\,)/\partial\psi^2$, $\beta$ is the flap angle, $I_\beta$ is the blade mass moment of inertia about the flapping hinge, $\Omega$ is the rotor speed and $M_\beta$ is the aerodynamic flapping moment, which is given by Eq. (34).

## 2.5. Summary of the Equations of Motion

The overall coupled system of blade-wake-airfoil ODEs is written in the implicit form:

$$\mathbf{f}\left(\mathbf{x}, \dot{\mathbf{x}}, \mathbf{u}; \psi\right) = \mathbf{0}. \tag{37}$$

The vector $\mathbf{f}$ is partitioned as:

$$\mathbf{f} = \left\{ \begin{array}{c} \mathbf{f}_{AC} \\ \mathbf{f}_{FW} \end{array} \right\} \tag{38}$$

where $\mathbf{f}_{FW}$ is the system of wake ODEs, and $\mathbf{f}_{AC}$ is the system of all the remaining ODEs. In turn, $\mathbf{f}_{AC}$ is partitioned as:

$$\mathbf{f}_{AC} = \left\{ \begin{array}{c} \mathbf{f}_{RB} \\ \mathbf{f}_{UA} \end{array} \right\} \tag{39}$$

The vector $\mathbf{f}_{RB}$ denotes the system of rotor blade flapping equations. It consists of Eq. (36) written once for each blade, e.g., a total of 8 first-order ODEs for a 4-bladed rotor. The vector $\mathbf{f}_{UA}$ denotes the system of unsteady aerodynamic equations. It consists of four ODEs, two from Eq. (20) and two from Eq. (22) for each blade cross section. Therefore, if the rotor has $N_b$ blades, and the unsteady aerodynamic model is written at $N_c$ cross sections for each blade, then the total number of ODEs in $\mathbf{f}_{UA}$ is $4N_bN_c$. The corresponding output equations, Eq. (21) and Eq. (23), complete the model.

The unsteady aerodynamic equations are coupled with the blade flap equations because they determine the local lift coefficient, and therefore the flap moment acting on the blade. They couple with the wake equations again by determining the spanwise distribution of blade lift, and therefore of circulation, which affects the strength of the tip vortex. Conversely, the blade flap equations and the wake equations couple with the unsteady aerodynamic equations by determining the angle of attack $\alpha$ in Eq. (21), and the change in vertical velocity $\Delta w_g$ in Eq. (23), respectively.

The state vector $\mathbf{x}$ is partitioned as:

$$\mathbf{x} = \left\{ \begin{array}{c} \mathbf{x}_{FW} \\ \mathbf{x}_{AC} \end{array} \right\} \tag{40}$$

where $\mathbf{x}_{FW}$ contains the states of the free-vortex wake. The vector $\mathbf{x}_{AC}$ contains all the other states of the model, and in the present study is defined as

$$\mathbf{x}_{AC} = \left\{ \begin{array}{c} \mathbf{x}_{RB} \\ \mathbf{x}_{UA} \end{array} \right\}. \tag{41}$$

The vector $\mathbf{x}_{RB}$ contains the rotor blade flapping states. For example, for a four-bladed rotor it is:

$$\mathbf{x}_{RB}^T = \left[ \overset{*}{\beta}_1 \; \overset{*}{\beta}_2 \; \overset{*}{\beta}_3 \; \overset{*}{\beta}_4 \;\; \beta_1 \; \beta_2 \; \beta_3 \; \beta_4 \right] \tag{42}$$

The vector $\mathbf{x}_{UA}$ contains the unsteady aerodynamic states. For a four-bladed rotor it is partitioned as:

$$\mathbf{x}_{RB}^T = \left[ \mathbf{x}_{UA1}^T \; \mathbf{x}_{UA2}^T \; \mathbf{x}_{UA3}^T \; \mathbf{x}_{UA4}^T \right] \tag{43}$$

where the numerical subscript denotes the blade. The vector $\mathbf{x}_{UAi}$ for the $i$-th blade in turn is partitioned as:

$$\mathbf{x}_{UAi}^T = \left[ \mathbf{x}_{UAi1}^T \; \mathbf{x}_{UAi2}^T \; \ldots \mathbf{x}_{UAin}^T \right] \tag{44}$$

where the second subscript denotes the cross-section. Finally, the vector $\mathbf{x}_{UAij}$ of aerodynamic states at the $j$-th cross-section of the $i$-th blade is given by:

$$x_{UAij}^T = \left[ x_1 \; x_2 \; z_1 \; z_2 \right]_{ij} \tag{45}$$

where $x_1$ and $x_2$, and $z_1$ and $z_2$, are the states that appear in Eq. (21) and Eq. (23), respectively. Therefore, if the rotor has $N_b$ blades, and the unsteady aerodynamic model is written at $N_c$ cross sections for each blade, then the total number of elements in $\mathbf{x}_{UA}$ is $4N_bN_c$.

## 3. Solution Techniques

### 3.1. Numerical Integration of the Equations

The ODEs making up the state-space free-vortex wake model can be integrated in time (or azimuth angle) with any ODE solver. These ODEs are in the explicit form $\dot{\mathbf{x}} = \mathbf{f}(\mathbf{x}, t)$, however, in the present study, they are implemented in the more general implicit form $\mathbf{f}(\dot{\mathbf{x}}, \mathbf{x}, t) = \mathbf{0}$. This reduces the number of suitable ODE solvers and increases the computational effort [13], but greatly simplifies the coupling with modern rotorcraft dynamic models that are based on nonlinear finite elements and multibody dynamics.

Two ODE solvers were used in the present study. The first is DASSL, Ref. [32], a variable-step, variable-order DAE solver based on backward difference formulas, which can solve a system of implicit ODEs as a special cases of DAEs with no algebraic equations. The second is the Hughes–Hilber–Taylor (HHT) method [33], which is a fixed-order integration scheme used to solve systems of second-order differential equations and is typically associated with structural dynamic calculations. The method was implemented in the version proposed by Negrut *et al.* for systems of simultaneous first- and second-order ODEs [34].

The wake equations are integrated in time to obtain two types of solution, namely, steady-state and transient solutions. The former are appropriate for steady-state flight conditions, and are obtained by starting the integration with some initial wake geometry, typically from a prescribed wake solution or from the free-vortex wake solution of a similar problem. The difference between the initial and the true solutions generates a numerical transient. The integration then continues until this transient dies out and a periodic solution is achieved as indicated by some convergence criterion. In the present study, the convergence criterion is based on the absolute change of the wake geometry between successive revolutions ($n$ and $n-1$), i.e.,

(46)
$$RMS_{n:n-1} = \sqrt{\frac{1}{3N_{vf}N_\zeta}\sum_{i=1}^{N_{vf}}\sum_{j=1}^{N_\zeta}\sum_{k=1}^{3}\left(r^n_{i,j,k} - r^{n-1}_{i,j,k}\right)^2}$$

which must be below some given value, $RMS_{n:n-1} < \epsilon$, to signify convergence. In some flight conditions a precisely periodic wake geometry does not exist, and the error decreases initially, but then oscillates in an aperiodic manner inside a convergence band. When this occurs, the integration is terminated arbitrarily, a few revolutions after the error has stopped decreasing monotonically.

The second type of solution is a truly transient solution, in which the flight condition is altered, for example, by a time-varying change in rotor controls. In this case, the governing ODEs are integrated starting from the steady-state solution, and until desired.

It should be pointed out that a by-product of the present state-space wake formulation is a new methodology for a true "tight" coupling between the free-wake model and the rotor-fuselage equations. In fact, they can all be solved simultaneously as a single system using the same ODE solver. Therefore, there is no need for the separate integration of wake and rotor-fuselage equations, with periodic resynchronizations of the solution (which is the basis of current "tight" coupling methodologies). Additionally, the MOL can be applied to most CFD problems of interest to the rotorcraft community, and therefore it can also provide a new methodology for true tight CFD/CSD coupling. In this case, however, particular care should be used in the generation of reduced-order models, as the baseline state-space models could be prohibitively large.

### 3.2. Linearized Models

With the free-vortex wake formulated as a system of ODEs, it is straightforward to extract a linearized state-space model, for example using conventional numerical perturbation techniques. Begin by setting to zero the first-order differential of $\mathbf{f}$:

(47)
$$\mathbf{0} = d\mathbf{f} = \left.\frac{\partial \mathbf{f}}{\partial \mathbf{x}}\right|_0 d\mathbf{x} + \left.\frac{\partial \mathbf{f}}{\partial \dot{\mathbf{x}}}\right|_0 d\dot{\mathbf{x}} + \left.\frac{\partial \mathbf{f}}{\partial \mathbf{u}}\right|_0 d\mathbf{u} + \left.\frac{\partial \mathbf{f}}{\partial \psi}\right|_0 d\psi$$

where the subscript "0" indicates that the derivatives are evaluated at a steady-state condition $\mathbf{x}(\psi) = \mathbf{x}_0(\psi)$, $\dot{\mathbf{x}}(\psi) = \dot{\mathbf{x}}_0(\psi)$, $\mathbf{u}(\psi) = \mathbf{u}_0(\psi)$, and $\psi = \psi_0$. In general, all matrices and vectors will be a function of blade azimuth $\psi$. Defining now:

(48)
$$\begin{aligned} A_1(\psi) &\stackrel{def}{=} \left.\frac{\partial \mathbf{f}}{\partial \mathbf{x}}\right|_0 & A_2(\psi) &\stackrel{def}{=} \left.\frac{\partial \mathbf{f}}{\partial \dot{\mathbf{x}}}\right|_0 \\ B_1(\psi) &\stackrel{def}{=} \left.\frac{\partial \mathbf{f}}{\partial \mathbf{u}}\right|_0 & \mathbf{F}_1(\psi) &\stackrel{def}{=} \left.\frac{\partial \mathbf{f}}{\partial \psi}\right|_0 \end{aligned}$$

and changing the infinitesimal increments $d(\ldots)$ to small finite increments $\Delta(\ldots)$, the linearized system can be rewritten as

(49)
$$A_1(\psi)\Delta\mathbf{x} + A_2(\psi)\Delta\dot{\mathbf{x}} + B_1(\psi)\Delta\mathbf{u} + \mathbf{F}_1(\psi)\Delta\psi = \mathbf{0}.$$

where all the terms can be obtained numerically, using finite-difference approximations. For example, using forward differences, the $i$-th column of the matrix $A(\psi)$ at the azimuth $\psi_k$ is given by:

(50)
$$\begin{aligned} \{A_1(\psi_k)\}_i &\stackrel{def}{=} \left.\frac{\partial \mathbf{f}}{\partial x_i}\right|_0 \approx \left.\frac{\Delta \mathbf{f}}{\Delta x_i}\right|_0 \\ &= \frac{\mathbf{f}\left(\mathbf{x}_0 + h\mathbf{e}_i, \dot{\mathbf{x}}_0, \mathbf{u}_0; \psi_k\right) - \mathbf{f}\left(\mathbf{x}_0, \dot{\mathbf{x}}_0, \mathbf{u}_0; \psi_k\right)}{h} \end{aligned}$$

where $h$ is a small increment, and $\mathbf{e}_i$ is a vector with all elements equal to zero except for the $i$-th, which is equal to one. The matrices $A_2(\psi_k)$ and $B_1(\psi_k)$, and the vector $\mathbf{F}_1(\psi_k)$ are calculated in the same way. Finally, Eq. (49) can be rewritten as

(51)
$$\Delta\dot{\mathbf{x}} = A(\psi)\Delta\mathbf{x} + B(\psi)\Delta\mathbf{u} + \mathbf{F}(\psi)\Delta\psi$$

with $A(\psi) = -A_2^{-1}(\psi)A_1(\psi)$, $B(\psi) = -A_2^{-1}(\psi)B_1(\psi)$, and $\mathbf{F} = A_2^{-1}(\psi)\mathbf{F}_1(\psi)$. The stability of the system can now be assessed by examining the eigenvalues of the $A$-matrix

averaged over one rotor revolution, or the characteristic exponents of Floquet theory if periodicity is taken into account.

The inflow $\lambda$ does not appear explicitly in the linearized model, although its effects are fully taken into account. If desired, explicit perturbation inflow information can be extracted by adding the equivalent of an output equation to Eq. (51), which would take the form:

$$\Delta\boldsymbol{\lambda} = C(\psi)\Delta\mathbf{x} + E(\psi)\Delta\psi \tag{52}$$

where the vector $\Delta\boldsymbol{\lambda}$ contains the inflow perturbations at a number of preassigned locations, e.g., at a series of spanwise cross-sections of the blade. In this case, the output matrix $C(\psi)$ and the vector $\mathbf{E}(\psi)$ could be obtained numerically, using finite-difference approximations, in the same way as for the state-space matrices $A(\psi)$ and $B(\psi)$. Because the inflow is calculated anyway as part of the extraction of $A(\psi)$ and $B(\psi)$, the matrix $C(\psi)$ and the vector $\mathbf{E}(\psi)$ can be calculated at the same time with minimum additional computational effort.

## 4. Reduced-Order Free-Vortex Wake

The application of the MOL to the governing wake equations can result in a large number of states. For example, if the wake of a four-bladed rotor is modeled using a single tip vortex per blade, and each vortex is discretized in segments of $\Delta\zeta$ = 5° wake age, and assumed to have a length equal to four rotor revolutions, or $\zeta$ = 1440°, then the total number of states will be 4 × 288 × 3 = 3456. Therefore, it is important to explore the possibility of reducing the order of the system of wake ODEs through appropriate coordinate transformations.

### 4.1. Basic Formulation

The order reduction is based on the assumption that the position of the vortex collocation points, and therefore, the geometry of the wake can be approximated by a linear combination of suitable shape functions:

$$r_k(\psi,\zeta) = \sum_{i=1}^{N_m} c_i(\psi)\phi_i(\zeta) \tag{53}$$

where $\phi_i(\zeta)$ is the $i$-th shape function, which depends only on wake age, $c_i(\psi)$ is the $i$-th generalized coordinate, which depends only on blade azimuth, and $N_m$ is the number of terms (or modes) in the series. The coordinates $c_i(\psi)$ become the state variables of the reduced-order model.

Equation (53) can be written for a discrete number of points in matrix form as

$$\begin{aligned}\mathbf{r}_k(\psi,\boldsymbol{\zeta}) &= \begin{bmatrix} \phi_1(\zeta_1) & \cdots & \phi_{N_m}(\zeta_1) \\ \vdots & \ddots & \vdots \\ \phi_1(\zeta_{N_\zeta}) & \cdots & \phi_{N_m}(\zeta_{N_\zeta}) \end{bmatrix} \begin{Bmatrix} c_1(\psi) \\ \vdots \\ c_{N_m}(\psi) \end{Bmatrix}_k \\ &= \mathbf{U}\mathbf{c}_k(\psi)\end{aligned} \tag{54}$$

Substituting this expression into Eq. (11) gives

$$\mathbf{U}\dot{\mathbf{c}}_k(\psi) = -[A_\zeta]\mathbf{U}\mathbf{c}_k(\psi) + \frac{1}{\Omega}\mathbf{V}_k[\mathbf{c}(\psi)] \tag{55}$$

where the notation $\mathbf{V}_k[\mathbf{c}(\psi)]$ simply indicates that the velocity vector $\mathbf{V}$ is now a function of the reduced coordinates $\mathbf{c}_k$. Premultiply by $\mathbf{U}^T$ to obtain

$$\left(\mathbf{U}^T\mathbf{U}\right)\dot{\mathbf{c}}_k(\psi) = -\mathbf{U}^T[A_\zeta]\mathbf{U}\mathbf{c}_k(\psi) + \frac{1}{\Omega}\mathbf{U}^T\mathbf{V}_k[\mathbf{c}(\psi)) \tag{56}$$

which is the reduced-order system of wake equations, of size $N_m$.

If the wake geometry $\mathbf{r}_k(0,\boldsymbol{\zeta})$ at $\psi = 0$ is known, then the initial conditions $\mathbf{c}_k(0)$ can be obtained from Eq. (54) with $\psi = 0$:

$$\left(\mathbf{U}^T\mathbf{U}\right)\mathbf{c}_k(0) = \mathbf{U}^T\mathbf{r}_k(0,\boldsymbol{\zeta}) \tag{57}$$

If $\mathbf{r}_k(0,\boldsymbol{\zeta})$ is not available, then the integration of the reduced-order wake ODEs can start from some approximate $\mathbf{c}_k(0)$, but the integration must continue until the numerical transient caused by the approximate initial conditions disappears, and a steady-state solution is found.

The boundary conditions, i.e., the conditions for zero wake age, can be found from Eq. (53) with $\zeta = 0$, i.e.,

$$\mathbf{r}_k(\psi,0) = \sum_{i=1}^{N_m} c_i(\psi)\phi_i(0) \tag{58}$$

or, in matrix form:

$$\mathbf{r}_k(\psi,0) = \begin{bmatrix} \phi_1(0) & \cdots & \phi_{N_m}(0) \end{bmatrix} \begin{Bmatrix} c_1(\psi) \\ \vdots \\ c_{N_m}(\psi) \end{Bmatrix}_k \tag{59}$$

This equation is used to satisfy the boundary conditions explicitly at each time step.

### 4.2. Basis Functions

Several types of shape functions were explored, including the eigenvector of the full-order linearized matrix $A(\psi)$, averaged over one rotor revolution, Chebyshev polynomials, and Fourier series.

Conventional Chebyshev polynomials $T_n(x)$ were used, i.e.,

$$\phi_n(\zeta) = T_n(x) = \cos(n\arccos(x)) \qquad x = 2\left(\frac{\zeta}{\zeta_{\max}}\right) - 1 \tag{60}$$

where $\zeta_{\max}$ is the total length of the trailed vortex.

The third set of shape functions consisted of Fourier series augmented by constant and linear terms. Two slightly different sets were used. In the first set, the period is the total length $[0, \zeta_{max}]$ of the trailed vortex:

$$\boldsymbol{\phi}_1 = \begin{Bmatrix} \phi_1(\zeta) \\ \phi_2(\zeta) \\ \vdots \\ \phi_{N_m/2}(\zeta) \\ \phi_{N_m/2+1}(\zeta) \\ \vdots \\ \phi_{N_m-1}(\zeta) \\ \phi_{N_m}(\zeta) \\ \vdots \end{Bmatrix} = \begin{Bmatrix} 1 \\ \cos(2\pi\zeta/\zeta_{max}) \\ \vdots \\ \cos[\pi\zeta\,(N_m-2)\,/\zeta_{max}] \\ \sin(2\pi\zeta/\zeta_{max}) \\ \vdots \\ \sin[\pi\zeta\,(N_m-2)\,/\zeta_{max}] \\ \zeta/\zeta_{max} \\ \vdots \end{Bmatrix} \tag{61}$$

In the second set the period is the length $[0, 2\pi]$ of one revolution of the trailed vortex:
(62)

$$\boldsymbol{\phi}_2 = \left\{ \begin{array}{c} \phi_1(\zeta) \\ \phi_2(\zeta) \\ \vdots \\ \phi_{N_m/2}(\zeta) \\ \phi_{N_m/2+1}(\zeta) \\ \vdots \\ \phi_{N_m-1}(\zeta) \\ \phi_{N_m}(\zeta) \\ \vdots \end{array} \right\} = \left\{ \begin{array}{c} 1 \\ \cos(\zeta) \\ \vdots \\ \cos[(N_m-2)\,\zeta/2] \\ \sin(\zeta) \\ \vdots \\ \sin[(N_m-2)\,\zeta/2] \\ \zeta/\zeta_{max} \\ \vdots \end{array} \right\}.$$

## 5. Results and Discussion

This section presents three types of numerical results obtained with the SSFW model, namely: (i) converged solutions for steady-state conditions; (ii) eigenvalues of the linearized system; (iii) transient wake response to pitch inputs. The converged and the transient solutions are compared with the finite-difference-based MFW, which is taken as the reference solution.

Unless specified otherwise, all the results in this paper refer to the coupled blade/wake/unsteady aerodynamic model with the following parameters: number of blades $N_b$ = 4; length of each trailed tip vortex $N_{WT}$ = 3 rotor revolutions, for a total wake age $\zeta_{\max}$ = 1080° and $N_\zeta$ = 216 collocation points, spaced $\Delta\zeta$ = 5° apart; and unsteady aerodynamic model applied at $N_c$ = 10 equally spaced spanwise stations for each blade. This results in 4 × 216 × 3 = 2,592 states for the wake, 160 states for unsteady aerodynamics, and 8 states for blade flapping, for a total of 2760 states.

Also, unless specified otherwise, the control angles for the hover and axial flight cases are: collective $\theta_0$ = 28°, lateral cyclic $\theta_{1c}$ = 0°, longitudinal $\theta_{1s}$ = 0°, and longitudinal shaft angle $\alpha_s$ = 0°. The corresponding values for the forward flight cases are: $\theta_0$ = 28°, $\theta_{1c}$ = 0°, $\theta_{1s}$ = -5°, and $\alpha_s$ = 5°. The blades have a linear twist, $\theta_{TW}$, or $-18°$. Note that these angles do not generally correspond to trimmed conditions. In fact, while the control angles are prescribed, rotor force and moment quantities, such as $C_T/\sigma$, take whatever values result from the converged wake solution with the given control. This was done because the primary objective for the results shown in this section was to evaluate the agreement between the new state-space wake and those of the existing finite-difference version. Any discrepancy between the two versions would have resulted in different trim solutions, and therefore in additional differences not directly related to the solution techniques.

In all figures, the results marked with "MOL" are those obtained using the state-space free-vortex wake. The results marked with "PC2B" are those obtained using the existing PC2B-based, finite-difference, MFW model.

### 5.1. Converged Wake Solutions

This section presents converged wake solutions, obtained by integrating the governing equations in time, starting from an initial geometry and proceeding until the change in geometry between successive revolutions falls below a certain threshold, see Eq. (46). The initial wake geometry is the rigid wake solution, Eqs. (14)-(16).

#### 5.1.1. Full-Order State-Space Wake

Five flight conditions were considered, namely, three hover and axial flight conditions ($\lambda_c$ = 0.05, 0, -0.025), and two forward flight conditions ($\mu$ = 0.15, 0.30).

The side views of the wake geometries obtained using the two methods are shown in Fig. 1 for the case of hover. The root mean square of the error (RMSE) is also shown in the figure to provide a global quantitative measure of the agreement between the state-space wake and the finite-difference wake. The results show that the agreement is excellent at the rotor disk and up to about half a rotor radius and then it deteriorates somewhat further downstream. These discrepancies coincide with increased vortex bundling, which, however, is not necessarily physical and can be caused by truncating the wake prematurely with no far wake boundary conditions, as in this example.

In the climb case, Fig. 2, the SSFW geometry shows better agreement with the MFW over the majority of the wake with a much lower RMSE. Only slight discrepancies are seen toward the bottom of the wake where very little bundling takes place. In the descent case (Fig. 3) on the other hand, the bundling intensifies as compared with the hover case, and the RMSE between the two methods is the highest for the hover and axial flight conditions, although there is still very good agreement at the rotor disk and just below it.

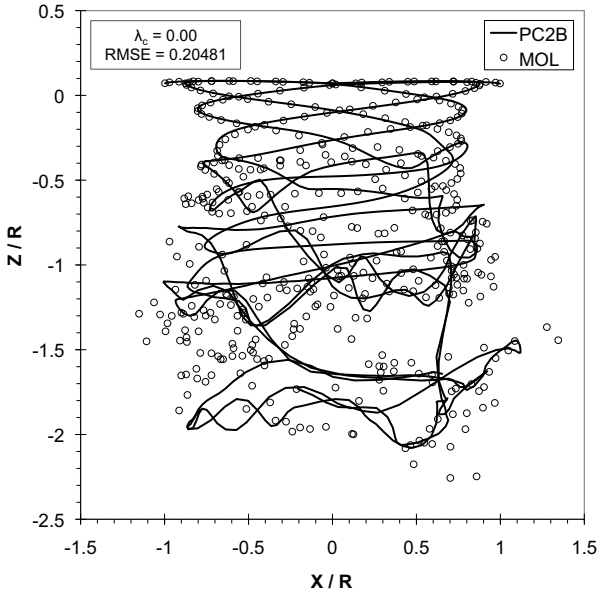


Figure 1: Full-order wake geometry in hover $\lambda_c$ = 0.0, compared with PC2B solution (solid line).

Figures 4 and 5 show, respectively, the wake geometries for forward flight at $\mu$ = 0.15 and 0.30. In each figure, the top, middle, and bottom plots show the side, rear, and top views, respectively. At $\mu$ = 0.15 there is excellent agreement within about half a rotor radius. Further downstream, the SSFW shows bigger differences with respect to the MFW. A better agreement, however, might be obtained by using longer trailed vortices and a finer discretization for

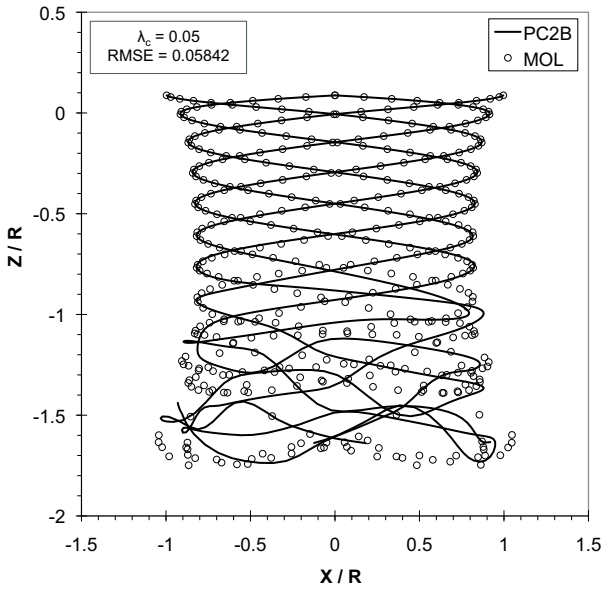


Figure 2: Full-order MOL wake geometry in a climb $\lambda_c$ = 0.05, compared with PC2B solution (solid line).

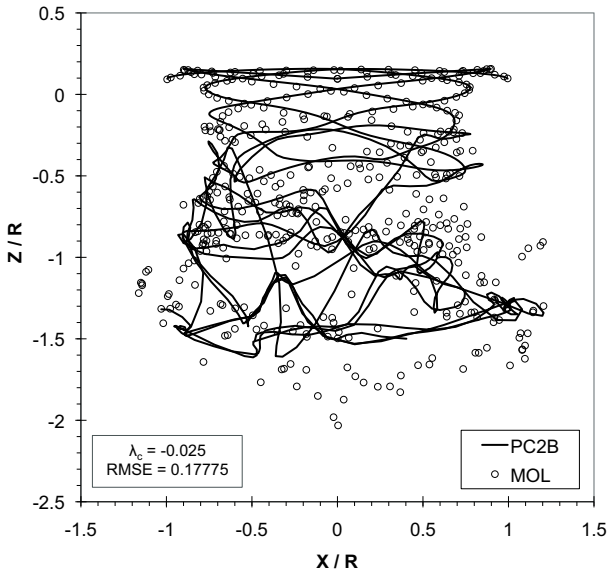


Figure 3: Full-order MOL wake geometry in a descent $\lambda_c$ = -0.025, compared with PC2B solution (solid line).

the SSFW. The trends for the $\mu$ = 0.30 case are similar, but the agreement between the two methods is much better, as indicated by the lower value of the RMSE.

From these results, it appears that the agreement between the two methods improves with increasing flight speed (in axial or forward flight). Higher free-stream velocities increase the separation distance between adjacent vortices, which weakens the contribution of the mutually-induced velocities acting on each vortex filament as compared the effects of the free-stream velocity. Therefore, the wake is more likely to converge to a periodic geometry, possesses fewer distortions from the initial rigid wake, and so it is easier to numerically capture the physical wake behavior.

Figures 6 through 10 show spanwise inflow distributions

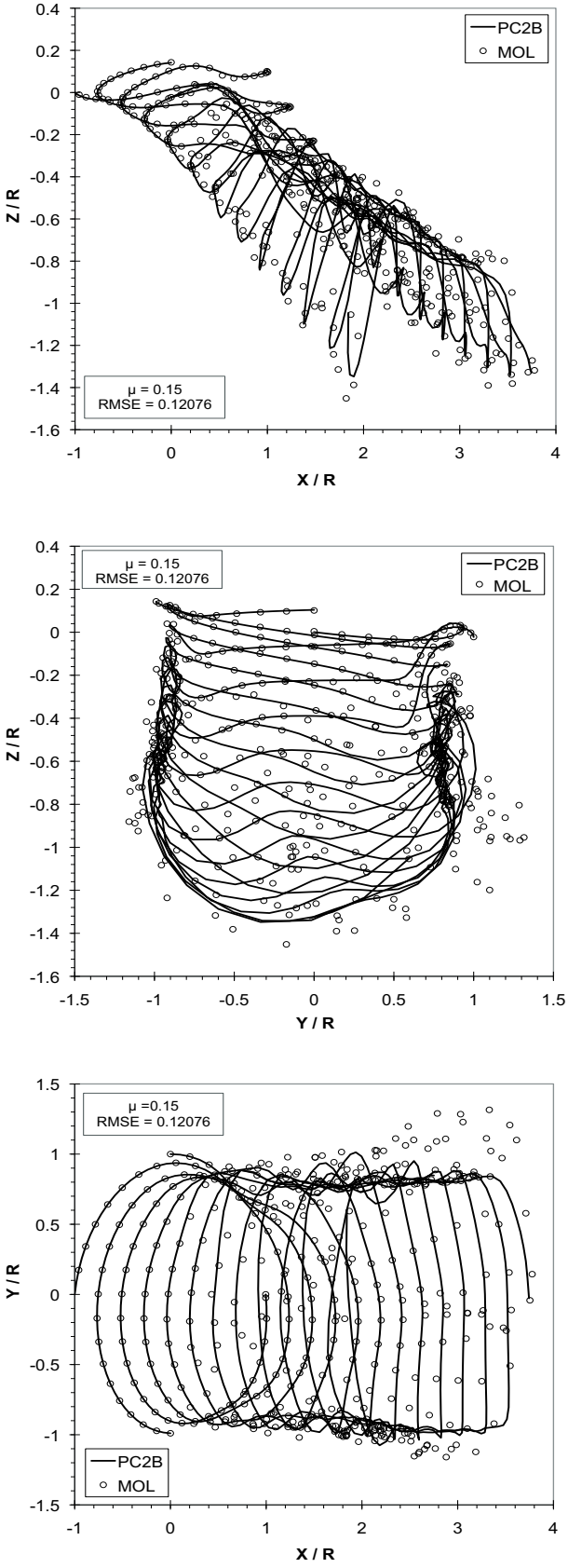


Figure 4: Full-order MOL wake geometry in forward flight $\mu$ = 0.15, compared with PC2B solution (solid line)

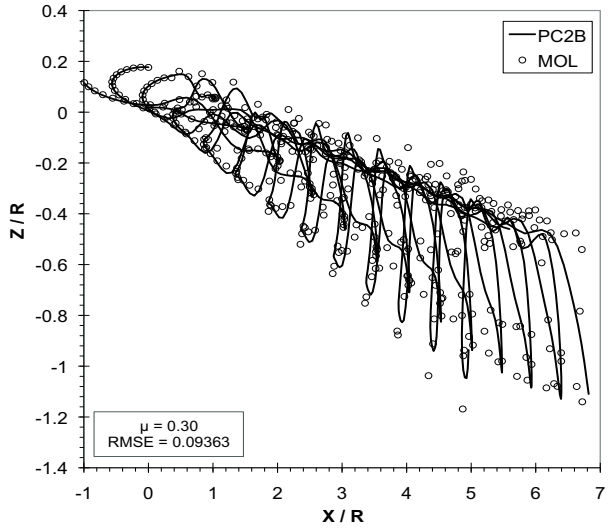


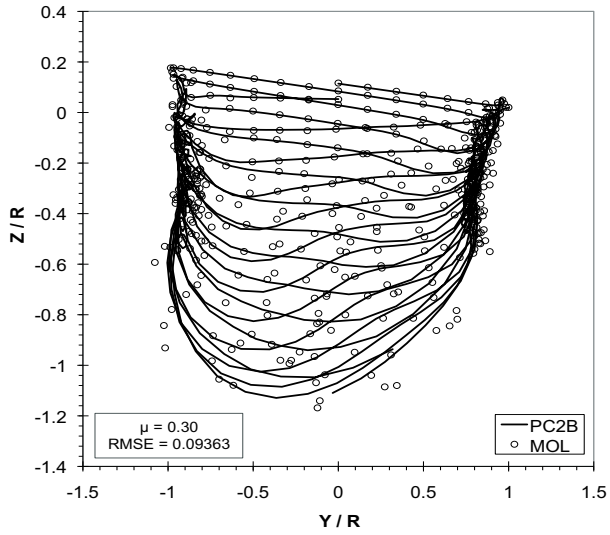


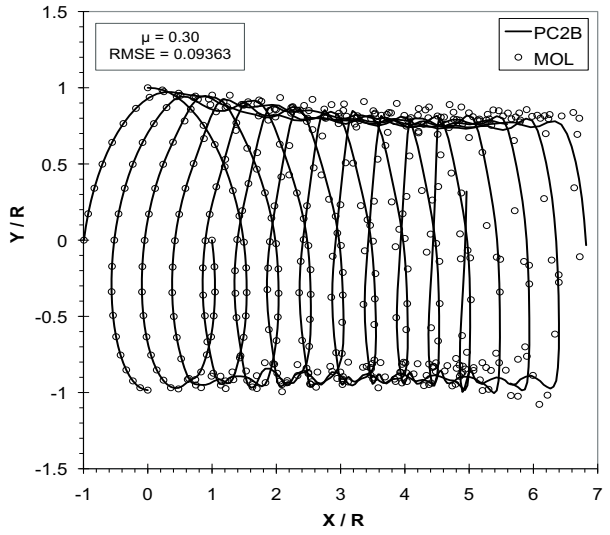


Figure 5: Full-order MOL wake geometry in forward flight $\mu$ = 0.30, compared with PC2B solution (solid line)

at 90-degree azimuth intervals for the five flight conditions and converged wake geometries previously shown in Figs. 1 through 5. The four curves for the hover and axial flight cases are essentially superimposed in the scale of the figures.

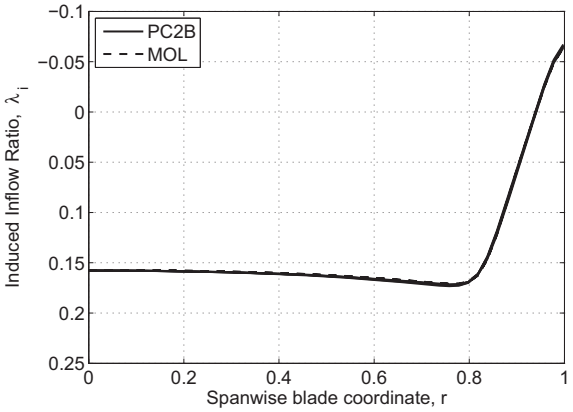


Figure 6: Spanwise inflow distribution for the full-order MOL and PC2B solutions in hover at 90° azimuth intervals.

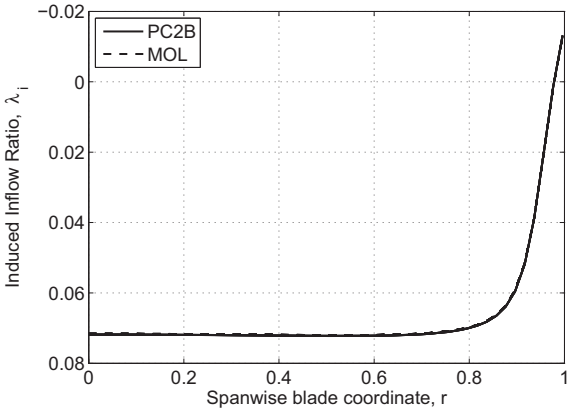


Figure 7: Spanwise inflow distribution for the full-order MOL and PC2B solutions in a climb with $\lambda_c$ = 0.05 at 90° azimuth intervals.

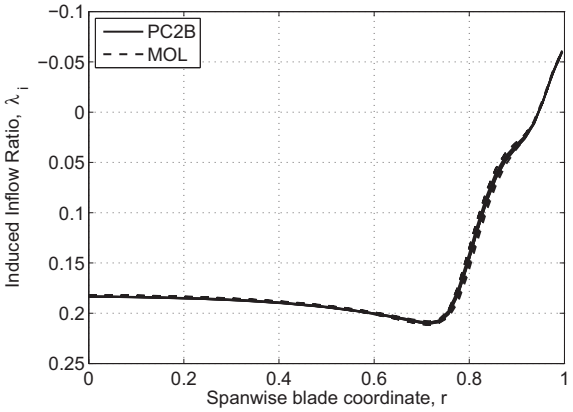


Figure 8: Spanwise inflow distribution for the full-order MOL and PC2B solutions in a descent with $\lambda_c$ = - 0.025 at 90° azimuth intervals.

Figures 6 through 10 show spanwise lift distributions at 90-degree azimuth intervals for the same five flight conditions and converged wake geometries. Again, the four

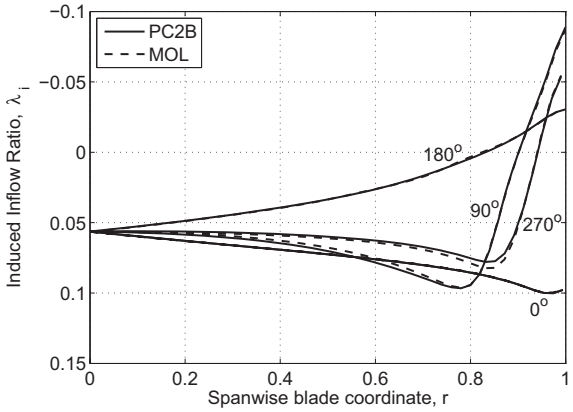


Figure 9: Spanwise inflow distribution for the full-order MOL and PC2B solutions in forward flight $\mu$ = 0.15 at 90° azimuth intervals.

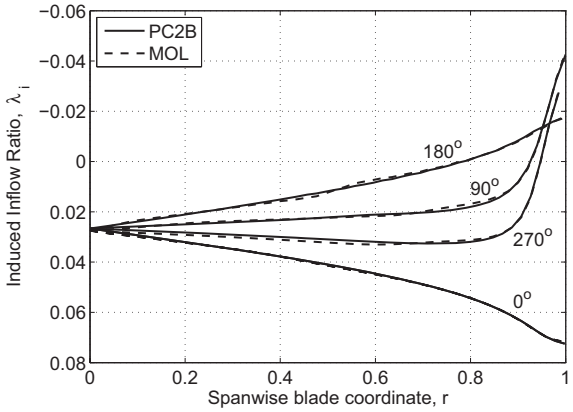


Figure 10: Spanwise inflow distribution for the full-order MOL and PC2B solutions in forward flight $\mu$ = 0.30 at 90° azimuth intervals.

curves for the hover and axial flight cases are superimposed in the scale of the figures.

Taken together, Figs. 6 through 15 clearly indicate that the differences between the SSFW and the MFW geometries in the downstream regions of the wake have a negligible influence on the spanwise lift and inflow distributions in all five flight conditions. The excellent agreement between the wake geometries up to a distance of at least half a rotor radius is sufficient to ensure nearly identical blade inflow and lift distributions.

### 5.1.2. Reduced-Order State-Space Wake

Three types of modes (or shape functions) were considered to reduce the order of the state-space wake model, namely, eigenvectors of the averaged $A(\psi)$ matrix, Chebyshev polynomials, and Fourier series. The results presented in this section all refer to the Fourier series based shape functions, which proved the most successful of the three.

As a preliminary step to actual wake geometry calculations, and to determine how many functions would be required to approximate the wake geometry, the wake vortices corresponding to MFW converged solutions for all five flight conditions were interpolated using the Fourier-based shape functions of Eq. (61). A single-bladed rotor was used

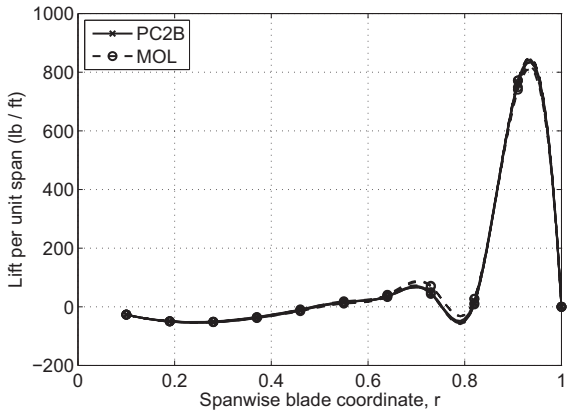


Figure 11: Spanwise lift distribution of the full-order MOL and PC2B solutions in hover at 90° azimuth intervals.

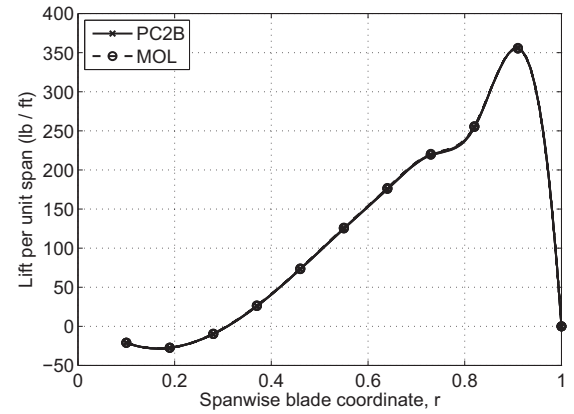


Figure 12: Spanwise lift distribution of the full-order MOL and PC2B solutions in climb $\lambda_c$ = 0.05 at 90° azimuth intervals.

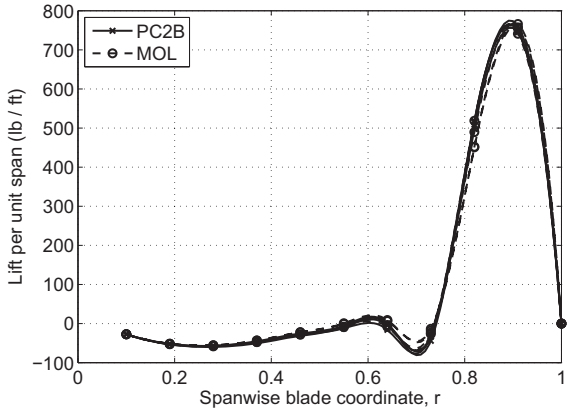


Figure 13: Spanwise lift distribution of the full-order MOL and PC2B solutions in descent $\lambda_c$ = -0.025 at 90° azimuth intervals.

for these preliminary calculations. The relative accuracy between the interpolated solution and PC2B solution for varying mode number is shown in Fig. 16 in terms of the RMSE. By inspection, the steep climb case has a low spatial (or wake age) frequency as indicated by its high accuracy at low mode number. The accuracy decreases and the spatial frequency increases when moving from hover to descent. In forward flight the error and spatial frequency reach their

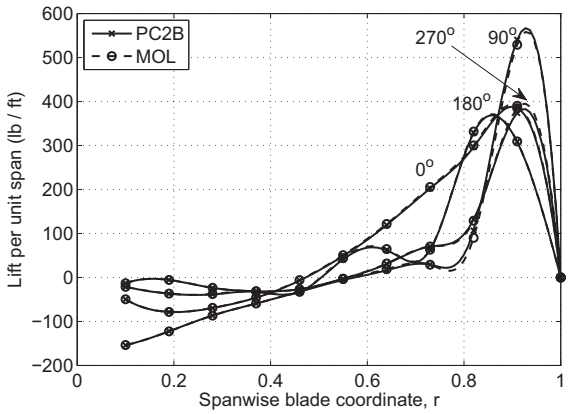


Figure 14: Spanwise lift distribution of the full-order MOL and PC2B solutions in forward flight $\mu = 0.15$ at 90° intervals around the azimuth.

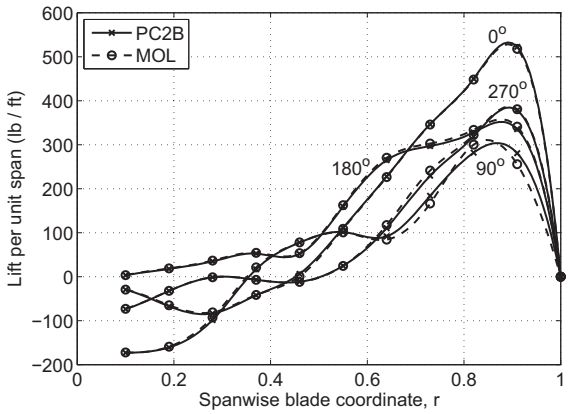


Figure 15: Spanwise lift distribution of the full-order MOL and PC2B solutions in forward flight $\mu = 0.30$ at 90° intervals around the azimuth.

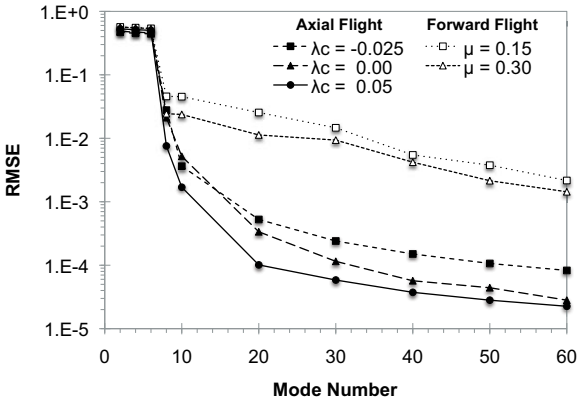


Figure 16: Root mean square of the interpolation error of converged PC2B geometries as a function of number of modes.

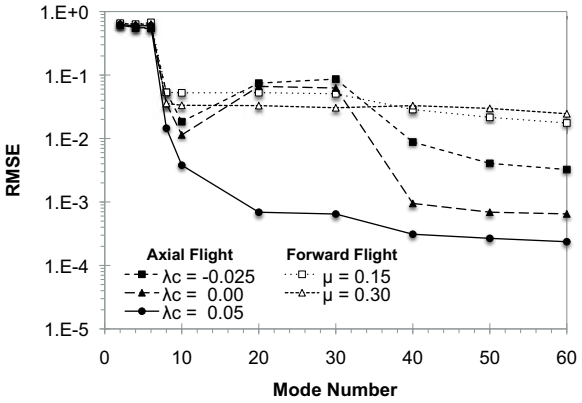


Figure 17: Root mean square of the error between the full-order MOL solution and reduced-order MOL solution as a function of number of modes.

highest values because of the proximity of vortices and the strengths of their interactions.

The RMSE between the full-order and reduced-order MOL solution for actual wake calculations, and for varying number of modes is shown in Fig. 17. The results cover the three hover and axial flight conditions, and the two forward flight conditions. There is a clear decrease in the error for all flight conditions around the eighth mode. This occurs because the frequency of the reduced-order formulation matches up exactly with the frequency of the boundary conditions. For example, three wake turns are used in this analysis, so for the wake geometry to match up with the one-per-rev boundary conditions then three harmonics (or 6 functions) plus a constant and a linear term are needed, for a total of eight modes. Increasing the number of modes slowly decreases the approximation error, although not always monotonically for hover and descending flight conditions.

Examples of reduced-order wake geometries in hover, axial and forward flight using the Fourier series-based shape functions can be seen in Figs. 18 through 24. The hover geometry is shown in Fig. 18 (for clarity, only one trailed vortex is shown). The 8-mode solution is not very accurate after the first revolution. The 20-mode solution is much closer, and the 40-mode solution is essentially indistinguishable from the full-order solution. A 40-mode solution for a four-bladed rotor consists of $4 \times 40 \times 3 = 480$ ODEs, compared with the 2592 ODEs of the full-order wake, i.e., a reduction of 81% of the number of states.

Fewer modes are needed to match the full-order climb geometry (Fig. 19) and just eight modes are sufficient. Conversely, slightly more modes than for the hover case are needed to capture precisely the wake geometry in the descending flight case, as shown in Fig. 20. In forward flight at $\mu = 0.15$, eight modes can easily capture the $x$ and $y$ displacements of the wake geometry, as shown in Fig. 21. As to the $z$-coordinate, 8 modes are sufficient to capture the general behavior of the vortex wake, but as many as 60 are needed to capture all the details (Fig. 22), which shows the $z$ displacements of the wake as a function of wake age, $\zeta$. The same behavior can be observed at $\mu = 0.30$, as shown in Figs. 23 and 24.

Taken together, Figs. 18 through 24 indicate that the number of modes required to capture the wake geometry varies not only with the flight condition, but also with the geometrical component of the vortex wake that is being approximated. The gross geometrical features can be captured with as few as four to eight modes, and this may be sufficient to study problems that are driven by integrated rotor quantities, such as flight dynamics problems. More

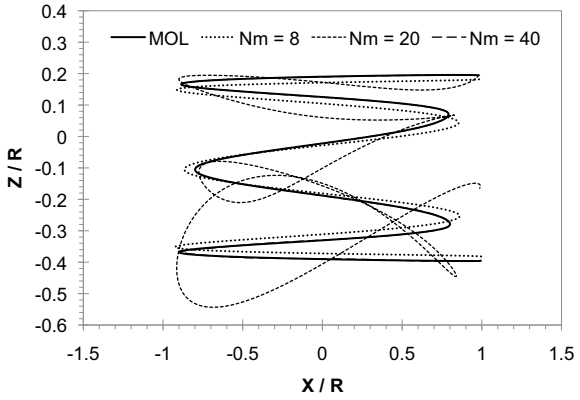


Figure 18: Reduced-order wake geometry in hover using Fourier based shape functions; solid line: full-order MOL solution, $\lambda_c$ = 0.0.

modes will be necessary for problems that require more accurate local descriptions, such as rotor vibration and loads predictions.

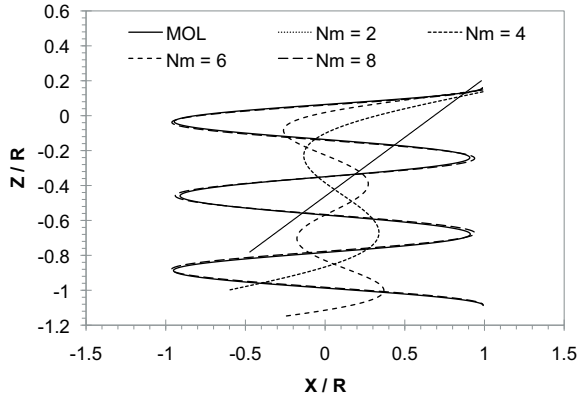


Figure 19: Reduced-order wake geometry in hover using Fourier based shape functions; solid line: full-order MOL solution, $\lambda_c$ = 0.05.

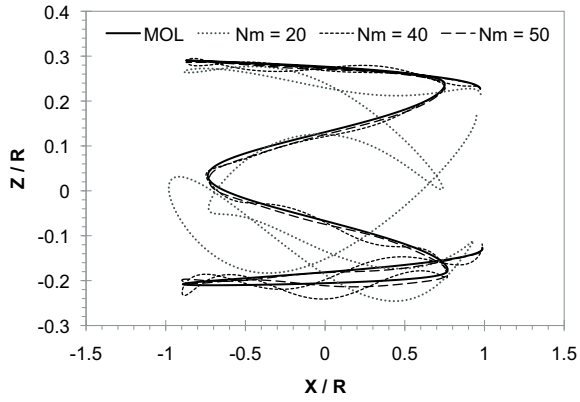


Figure 20: Reduced-order wake geometry in hover using Fourier based shape functions; solid line: full-order MOL solution, $\lambda_c$ = -0.025.

Figures 25 through 29 show converged wake geometries computed using a reduced-order model based on the second type of Fourier series-based shape functions given

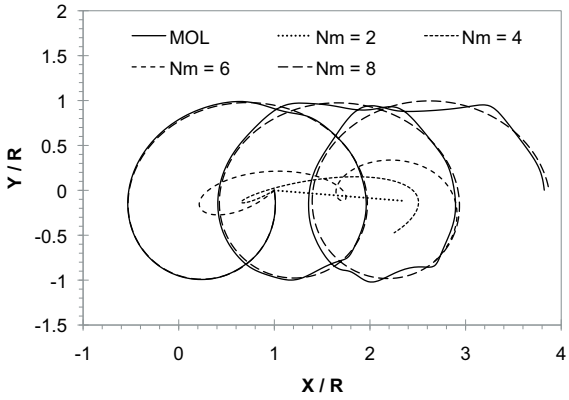


Figure 21: Reduced-order wake geometry in forward flight using Fourier based shape functions; solid line: full-order MOL solution, $\mu$ = 0.15.

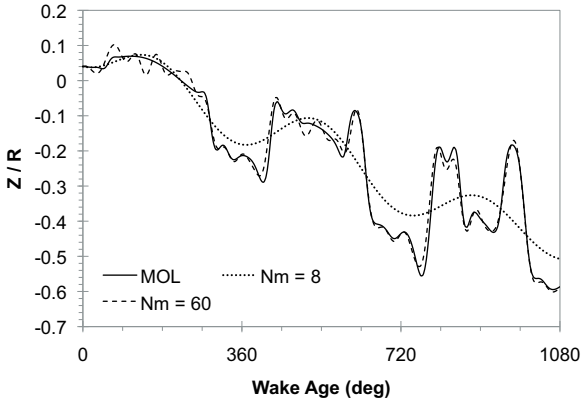


Figure 22: Reduced-order wake geometry in forward flight using Fourier based shape functions; solid line: full-order MOL solution, $\mu$ = 0.15.

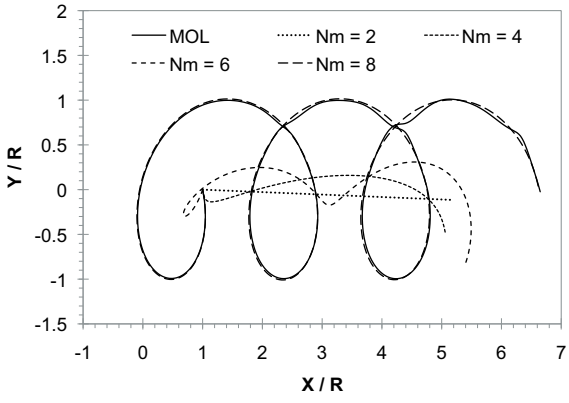


Figure 23: Reduced-order wake geometry in forward flight using Fourier based shape functions; solid line: full-order MOL solution, $\mu$ = 0.30.

by Eq. (62). These functions have the fundamental period $T = 2\pi$, i.e., only one rotor revolution instead of $T$ equal to the full length of the trailed vortex, $T = 6\pi$, as in the previous set of results. Each figure shows the $x$-, $y$-, and $z$-components of the vortex wake displacements as a function of wake age for each of the five flight conditions analyzed in

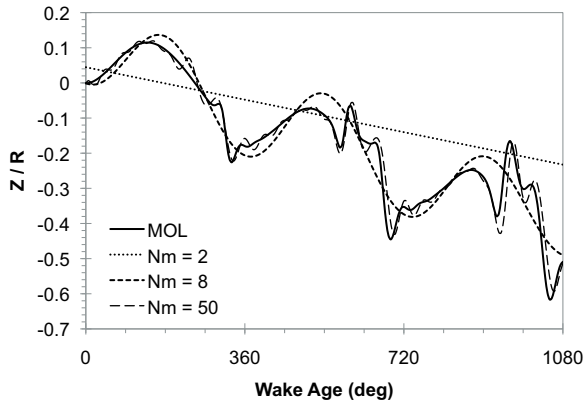


Figure 24: Reduced-order wake geometry in forward flight using Fourier based shape functions; solid line: full-order MOL solution, $\mu$ = 0.30.

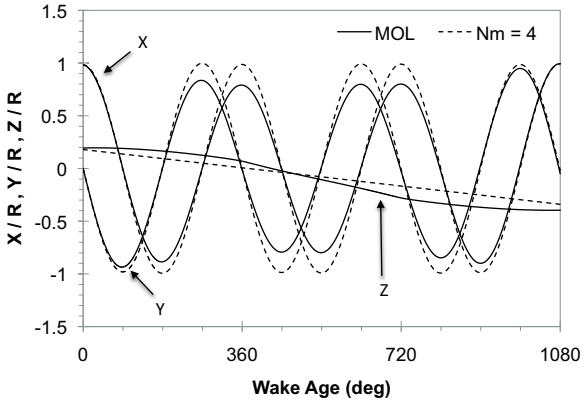


Figure 25: Reduced-order wake geometry in hover using Fourier based shape functions with period $T = 2\pi$; solid line: full-order MOL solution, hover.

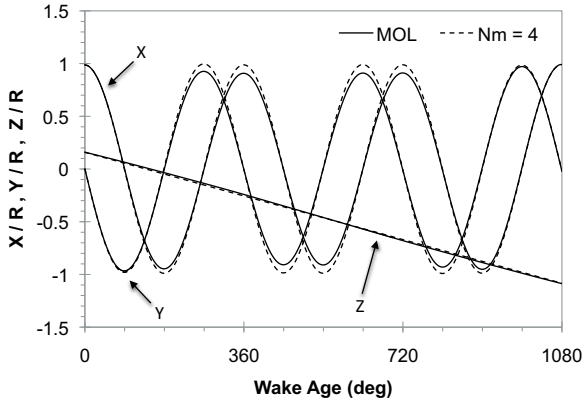


Figure 26: Reduced-order wake geometry in hover using Fourier based shape functions with period $T = 2\pi$; solid line: full-order MOL solution, $\lambda_c$ = 0.05.

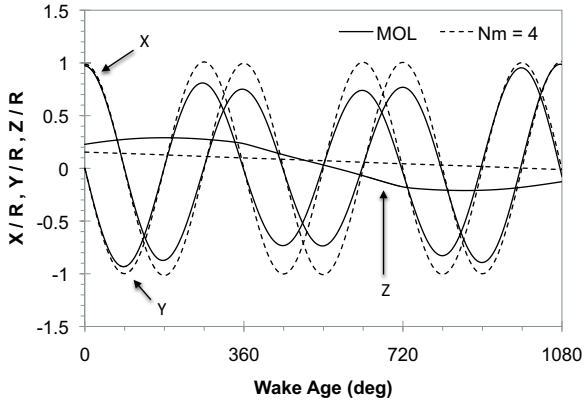


Figure 27: Reduced-order wake geometry in hover using Fourier based shape functions with period $T = 2\pi$; solid line: full-order MOL solution, $\lambda_c$ = -0.025

this section. The figures show the special case of 4 modes, i.e., 4 ODEs per coordinate. In all cases, this very low-order model captures well the $x$ and $y$ coordinates of the vortices, and the basic behavior in the $z$ coordinate. This shows that, through a careful selection of the family of shape functions, it is possible to obtain very low-order free-vortex wake models of good fidelity.

## 5.2. Eigenvalues

With the free-vortex wake in state-space form, it is straightforward to extract linearized dynamic models. This section presents eigenvalues in the five flight conditions used throughout the paper.

Full-order, SSFW eigenvalues (or poles) are shown in Figs. 30 through 34 for hover, climb, descent, and forward flight at $\mu$ = 0.15 and 0.30. In all cases, the general arrangement of the poles is qualitatively similar to that of the poles of the numerical scheme used to discretize $\zeta$ in the method of lines. In Ref. [13], where simple rigid wake solutions were calculated, this trend was clear. In the present study, the effect of the nonlinearities and the couplings introduced by the velocity vector $\mathbf{V}[\mathbf{r}(\psi, \zeta)]$ on the right-hand-side of the governing wake equations (Eq. (1)) is to slightly alter this pattern. As vortex bundling and mutual interactions become stronger, as in descent (Fig. 32) and low-speed, forward flight (Fig. 33) flight conditions, the eigenvalues become much more diffuse and spread out. For the forward flight cases, it should be pointed out that the poles are those of the state matrix $A(\psi)$ averaged over one revolution, i.e., the effects of periodicity have been neglected. The strength of such effects, and therefore the possible need for Floquet theory, will be explored in upcoming phases of the present research.

It should also be noted that the poles in the figures are *coupled* wake/unsteady aerodynamics/rotor flapping. These are the first such poles presented in the literature, and are made possible by the availability of the new state-space free-vortex wake model.

Reduced-order poles have also been computed for all five flight conditions, and increasing number of modes, but the results are not shown here for brevity. In general, the reduced-order poles follow the same pattern as the full-order poles. For small numbers of modes, the poles closest to the origin are retained. As the number of modes increase, more poles appear away from the origin, progressively forming the same circular pattern as the full-order case

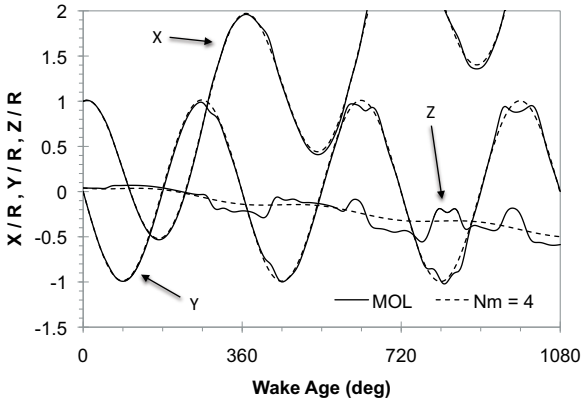


Figure 28: Reduced-order wake geometry in forward flight using Fourier based shape functions with period $T = 2\pi$; solid line: full-order MOL solution, $\mu$ = 0.15.

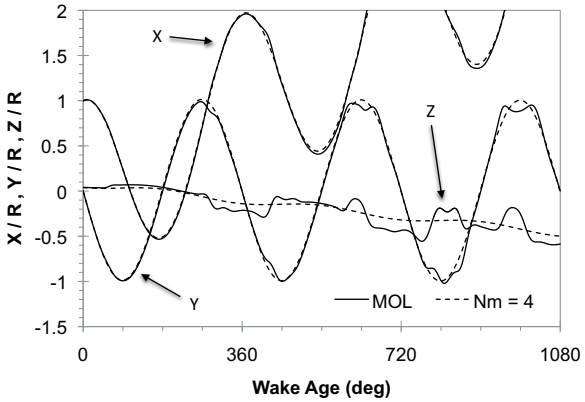


Figure 29: Reduced-order wake geometry in forward flight using Fourier based shape functions with period $T = 2\pi$; solid line: full-order MOL solution, $\mu$ = 0.30

### 5.3. Transient Solution

The coupled rotor/free-vortex wake/state-space model was compared with the equivalent finite-difference model for a transient response case. In this case, the collective was ramped from 0° to 12° at a pitch rate of 200°/sec (note that these conditions are similar to those of the classic test by Carpenter and Fridovich [35]). The time history of the rotor thrust during the transient is shown in Fig. 35. The full-order SSFW and MFW solution are seen to be in nearly perfect agreement. The reduced-order solution with 60 modes matches very well the full-order response except for some small discrepancies in the second following the end of the thrust transient (from about 1.5 to about 2.5 sec) and some high frequency oscillations toward the end of the simulation. The solution with 8 modes is also in reasonably good agreement. The solution with 4 modes misses the $C_T$ drop at the end of the transient, but still captures the first portion of the transient and the peak value.

## 6. Conclusions

This paper has presented the initial development of a free-vortex wake model in state-space form. Because it is based on vortex theory the model is more rigorous than momentum-based theories for all applications for which an accurate, first-principles representation of the details of the rotor wake is necessary. With the new state-space model, free-vortex wake poles can now be extracted, both for the uncoupled (wake only) and coupled (wake, rotor, and unsteady aerodynamics) cases. Furthermore, free-vortex wake modeling can now be included in all the applications that require rotorcraft models in the mathematical form $\dot{\mathbf{x}} = A\mathbf{x} + B\mathbf{u}$, such as aeroelastic stability analyses, handling qualities studies

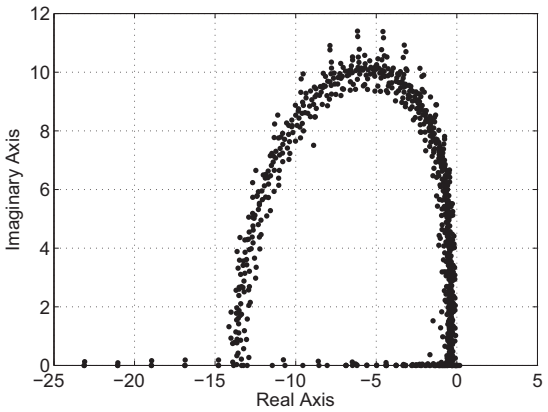


Figure 30: Eigenvalues of the full-order MOL solution in hover.

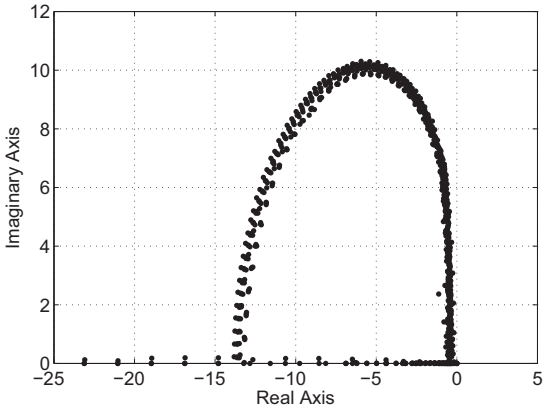


Figure 31: Eigenvalues of the full-order MOL solution in climb $\lambda_c$ = 0.05.

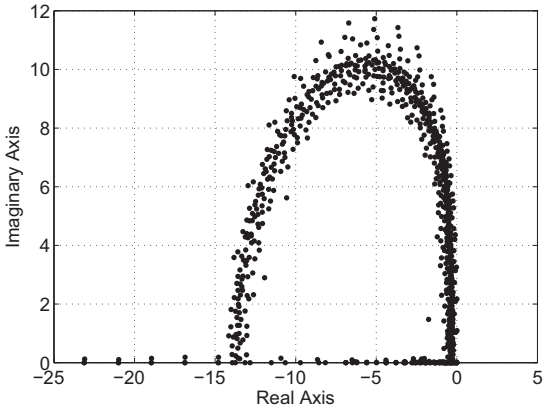


Figure 32: Eigenvalues of the full-order MOL solution in descent $\lambda_c$ = -0.025.

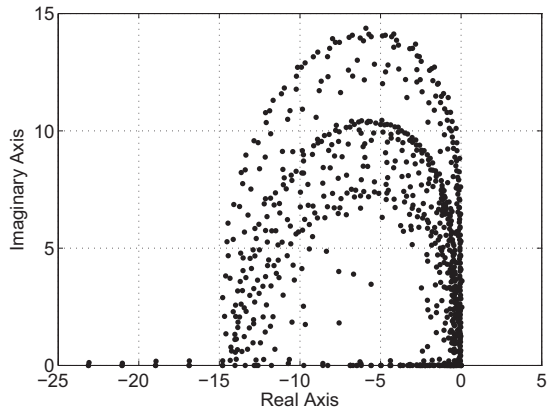


Figure 33: Eigenvalues of the full-order MOL solution in forward flight $\mu$ = 0.15.

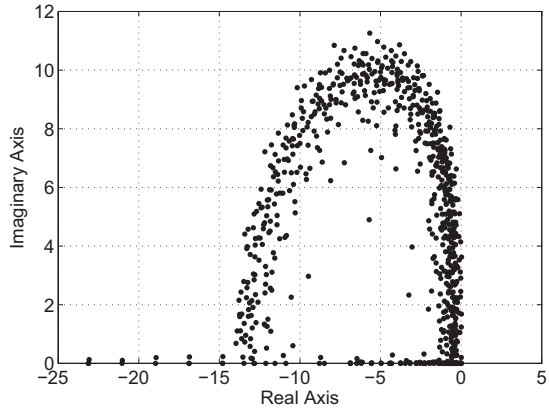


Figure 34: Eigenvalues of the full-order MOL solution in forward flight $\mu$ = 0.30.

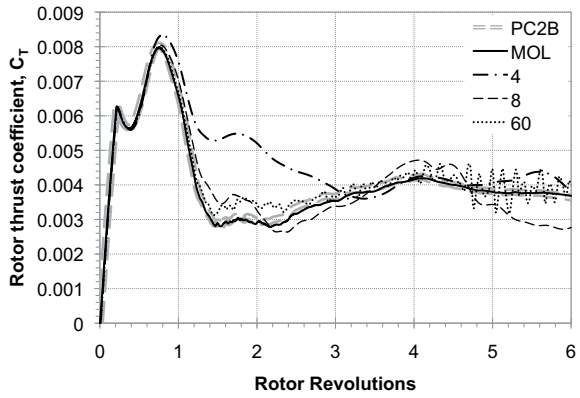


Figure 35: Rotor $C_T$ response to a ramp change in collective at 200 °/second; PC2B, full-order MOL and reduced-order MOL solutions.

(poles, bandwidth/delay), flight control system design, and active rotor control.

The main conclusions from the study are:

1. The Method-of-Lines is a viable methodology to formulate rotor free-vortex wake models in state-space form, starting from the governing equations of the vortex wake written in partial differential equation form.
2. Good agreement of wake geometry with finite-difference solutions near the rotor disk can be obtained, whereas away from the rotor disk the quality of the agreement depends on flight condition, solution method, and other solution details.
3. Excellent agreement of blade spanwise distributions of inflow and lift can be achieved, even in case of wake geometry mismatches away from the rotor disk.
4. No numerical convergence problems appear to exist, in that the numerical solution did not become unstable for any flight conditions, including hovering flight.
5. Excellent agreement with finite-difference solution can be obtained for transient wake conditions such as flight maneuvers.
6. Substantial reductions in the size of the state-space free-vortex wake model can be achieved with simple Fourier series-based transformations. However, the number of ODEs required depends on the application and the complexity of the wake geometry .

## 7. Acknowledgments

This research was sponsored by the National Aeronautics and Space Administration under NASA Ames Cooperative Agreement NNX07AP32A. The Technical Monitor was Dr. William G. Warmbrodt.

## References

[1] Fletcher, J. W., and Tischler, M. B., “Improving Helicopter Flight Mechanics Models with Laser Measurements of Blade Flapping, American Helicopter Society 53rd Annual Forum Proceedings, Virginia Beach, VA, April 1997, pp. 1467–1994.

[2] Rosen, A., Yaffe, R., Mansur, M. H., and Tischler, M. B., “Methods for Improving the Modeling of Rotor Aerodynamics for Flight Mechanics Purposes, American Helicopter Society 54th Annual Forum Proceedings, Washington, DC, May 1998, pp. 1337–1355.

[3] Mansur, M. H., and Tischler, M. B., “An Empirical Correction for Improving Off-Axes Responses in Flight Mechanics Helicopter Models, *Journal of the American Helicopter Society*, Vol. 43, No. 2, April 1998, pp. 94–102.

[4] Pitt, D. M., and Peters, D. A., “Theoretical Prediction of Dynamic Inflow Derivatives,” *Vertica*, Vol. 5, No. 1, 1981, pp. 21–34.

[5] Peters, D. A., and He, C.-J., “Correlation of Measured Induced Velocities with a Finite-State Wake Model,” *Journal of the American Helicopter Society*, Vol. 36, No. 3, July 1991, pp. 59–70.

[6] Joglekar, M., and Loewy, R., “An Actuator-Disc Analysis of Helicopter Wake Geometry and the Corresponding Blade Response, USAAVLABS Technical Report 69-66, December 1970.

[7] Line, A. J., and Brown, R. E., “High Resolution Wake Modeling Using A Semi- Lagrangian Adaptive Grid Formulation,” 29th European Rotorcraft Forum Proceedings, Friedrichshafen, Germany, September 2003.

[8] Johnson, W., “Rotorcraft Aerodynamics Models for a Comprehensive Analysis,” American Helicopter Society 54th Annual Forum Proceedings, Washington, DC, May 1998.

[9] Bhagwat, M. J., and Leishman, J. G., “Rotor Aerodynamics During Maneuvering Flight using a Time-Accurate Free-Vortex Wake,” *Journal of the American Helicopter Society*, Vol. 48, No. 3, July 2003, pp. 143–158.

[10] Johnson, W., Time-Domain Unsteady Aerodynamics of Rotors with Complex Wake Configurations, *Vertica*, Vol. 12, No. 1/2, January 1988, pp. 83–100.

[11] Johnson, W., “Feasibility Investigation of General Time-Domain Unsteady Aerodynamics of Rotors,” NASA CR-177570, October 1990.

[12] Miller, R. H., “Rotor Blade Harmonic Air Loading,” *AIAA Journal*, Vol. 2, No. 7, July 1964, pp. 1254–1269.

[13] Celi, R., “State-Space Representation of Vortex Wakes By the Method of Lines,” *Journal of the American Helicopter Society*, Vol. 50, No. 2, April 2005, pp. 195–205.

[14] Notz, P. K., and Basaran, O., “Dynamics and Breakup of a Contracting Liquid Filament,” *Journal of Fluid Mechanics*, Vol. 152, 2004, pp. 223–256.

[15] Tiwari, S., “Application of the Method of Lines for Solution of the Navier–Stokes Equations Using Nonuniform Grid Distributions,” *Applied Numerical Modeling*, San Diego, CA, Univelt, Inc., 1986, pp. 759–765.

[16] Nishida, H., “Direct Numerical Simulation of Incompressible Homogeneous Isotropic Turbulence Using Compressible Navier–Stokes Equations,” Special Publication of National Aerospace Laboratory, Japan, 1994, pp. 189–194

[17] Tokunaga, H., “Numerical Simulation of Transient Turbulent Flows by Vorticity-Vector Potential Simulation,” ISCFD Nagoya 1989 - International Symposium on Computational Fluid Dynamics, 3rd, Nagoya, Japan, August 1989, pp. 209–214.

[18] Tokunaga, H., Yoyedat, K., and Satofuta, N., “Direct Simulations of Three-Dimensional Flows using Generalized Vector Potential Method,” 10th AIAA Computational Fluid Dynamics Conference, Honolulu, HI, June 1991, pp. 937–946.

[19] Goman, M., and Khrabrov, A., “State-Space Representation of Aerodynamic Characteristics of an Aircraft at High Angles of Attack”. *Journal of Aircraft*, Vol. 3, No. 5, September–October 1994, pp. 1109–1115.

[20] Liao, B., and Zhu, J., “A Low-Order Nonlinear State-Space Model for Delta Wing Leading Edge Vortices,” AIAA Guidance, Navigation, and Control Conference and Exhibit, Keystone, CO, August 2006.

[21] Gordon, B., Pakmehr, M., and Rabbath, C., “State-Space Modeling and Identification of Delta Wing Vortex-Coupled Roll Dynamics,” *Journal of Aircraft*, Vol. 46, No. 1, January–February 2009, pp. 36–45.

[22] Tang, D., Henry, J. K., and Dowell, E. H., “Limit Cycle Oscillations of Delta Wing Models in Low Subsonic Flow’,’ *AIAA Journal* Vol. 32, No. 12, December 1994, pp. 2162–2172.

[23] Hall, K., “Eigenanalysis of Unsteady Flows About Airfoils, Cascades, and Wings,” *AIAA Journal* Vol. 32, No. 12, December 1994, pp. 2426–2432.

[24] E.H. Dowell, H.C. Curtis, R.H. Scanlan, and F. Sisto, *A Modern course in Aeroelasticity*, Kluwer Academic Publishers, 2004, Chapter 12.

[25] Krasny, R., “A study of Singularity Formation in a Vortex Sheet by the Point-Vortex Approximation,” *Journal of Fluid Mechanics*, Vol. 167, 1986, pp. 65–93.

[26] Michelin, S., and Llewellyn Smith, S. G., “An Unsteady Point Vortex Method for Coupled Fluid-Solid Problems,” *Theoretical and Computational Fluid Dynamics*, Vol. 23, No. 2, 2009, pp. 127-153.

[27] Bhagwat, M. J., and Leishman, J. G., “Time-Accurate Modeling of Rotor Wakes Using a Free-Vortex Wake Method,” 18th AIAA Applied Aerodynamics Conference Denver, CO, Vol. 1, August 2000, pp. 236–246.

[28] Bagai, A., and Leishman, J.G., “Rotor Free-Wake Modeling Using a Pseudo-Implicit Technique—Including Comparison with Experimental Data,” *Journal of the American Helicopter Society*, Vol. 40, No. 3, July 1995, pp. 29–41.

[29] Ribera, M., and Celi, R., “Simulation Modeling of Unsteady Maneuvers Using a Time-Accurate Free Wake,” American Helicopter Society 60th Annual Forum Proceedings, May 2004.

[30] Leishman, J. G., *Principles of Helicopter Aerodynamics, Second Edition*, Cambridge University Press, New York, NY, 2006.

[31] Schiesser, W. E., *The Numerical Method of Lines: Integration of Partial Differential Equations*, Academic Press, San Diego, CA, 1991.

[32] Brenan, K. E., Campbell, S. L., and Petzold, L. R., *The Numerical Solution of Initial Value Problems Using Differential-Algebraic Equations*, Elsevier Science Publishing Co., New York, NY, 1989.

[33] Hilber, H. M., Hughes, T. J. R., and Taylor, R. L., “Improved Numerical Dissipation for Time Integration Algorithms in Structural Dynamics,” *Earthquake Engineering and Structural Dynamics*, Vol. 5, 1977, pp. 283–292.

[34] Negrut, D., Rampalli, R., Ottarsson, G., and Sajdak, A., “On an Implementation of the Hilber-Hughes-Taylor Method in the Context of Index 3 Differential-Algebraic Equations of Multibody Dynamics,” *ASME Journal of Computational and Nonlinear Dynamics*, Vol. 2, No. 1, 2007, pp. 73–85.

[35] Carpenter, P. J., and Fridovich, B., ”Effect of A Rapid Blade- Pitch Increase on the Thrust and Induced-Velocity Response of a Full-Scale Helicopter Rotor,” NACA Technical Report TN 3044, November 1953.